University of Bucharest - Faculty of Physics

Ab initio study of q-1D würtzite semiconductor nanostructures

Master's Dissertation

Author:
Tudor Luca MITRAN

Coordinators:
Conf. Dr. Lucian ION
Dr. Alexandru G. NEMNES

Bucharest - June 2010

Contents

Chapter 1

Introduction

Because of the recent expansion of our technology towards the nanoscale, we are currently witnessing a growing demand of accurate simulation and prediction methods for advanced materials and micro or nano structures, or for what is known as the field of quantum chemistry. The quantum-mechanical approach that is needed to accurately describe multi-particle systems is out of reach for an analytical treatment (except for a very limited number of special cases) and we must make intensive use of numerical methods in order to reach our goal. The main limiting factor of the current numerical methods is the access to finite computational resources and, although the growth rate of computer performance available is rapidly rising, we still need to improve the theoretical model and the numerical methods that are being used in order to gain an insight in the behavior of structures that are comprised of more than just a couple of atoms. There are numerous examples of theoretical quantum-chemistry models being used in simulations, but they can all be divided between the *ab initio* or semi-empirical classes (the first making use only of fundamental physical constants and the latter allowing for the introduction of certain experimental results). The following material refers exclusively to *ab initio* computational methods. Some of the most popular general *ab initio* approaches are: Hartree-Fock (HF) and post Hartree-Fock (pHF) methods, quantum Monte Carlo (qMC) and the Density Functional (DFT - Density Functional Theory). Hartree-Fock and post Hartree-Fock are both approximate self-consistent variational methods used to determine the ground state wave-function and the ground-state energy of quantum many-body systems, the main difference between the two being the fact that the latter uses a linear combination of Slater determinants in order to represent the wave-function, in contrast to the single determinant used in the case of Hartree-Fock, which means that it also takes into account the electron correlation and leads to better accuracy. Quantum Monte Carlo methods imply a sort of variational 'guessing' problem and are considered the most accurate methods available for medium-sized systems (around some tens of electrons). All of the thee methods metioned above unfortunately fail to scale linearly with the size of the system, i.e. the number of electrons (N): HF and pHF methods usually scale as N^3 and qMC as N^2 [1].

Methods belonging to the last class, DFT, however, can scale linearly with the system size, and one such example is that of the software package used and described here: SIESTA (Spanish Initiative for Electronic Simulations with Thousands of Atoms), which can be used to model realistic sized systems, from nanostructures to bulk materials.

1.1 Motivation

Although there are numerous types of interesting and important nano-metric structures that could have been studied by the use of DFT method, this thesis is particularly directed towards the investigation of the general electronic properties of würtzite semiconductor nano-tubes and nano-wires. The reason for this choice is the fact that these types of structures are currently being used in prototype and consumer-grade electronic devices (like solar cells electrodes, magnetic and electric nano-sensors and nano-transistors) and even more purposes have been envisioned for them in the near future. It is also worth mentioning that certain features that are specific to the numerical approach that lies behind the SIESTA package make it most suitable for structures as the ones presented here (spatially isolated non-interacting nanowires and nanotubes) because the empty space that must be placed between them as a consequence of the Born-von Karman boundary conditions is almost 'free' from the computational standpoint.

The aim of this work is to investigate the changes that take place in the electronic and phononic properties of the material when switching from bulk boron nitride (BN) to quasi one-dimensional würtzite structures. Although BN might not seem a suitable material for electronic applications because of its high band-gap (4.5-5.5 eV), the presence of surfaces is expected to lower the gap energy. This study tackles a number of different sized nanowires and nanotubes and attempts to capture some of the effect of varying the external and internal radii, without attempting to be an exhaustive study of such properties. An investigation has also been carried out in order to find a better suited way of treating the surface of such structures. It must be said that the q-1D structures mentioned above were of a würtzite structure, and in order to carry out a better characterization, they have been compared to the much different but well know rolled grapheen-sheet BN nano-tubes. Another point of interest was that of phonon dispersion in nano-tubes and nano-wires and investigations in this direction were carried out for a few structures of würtzite and graphene structures in order to detect deviations from the known bulk behavior.

Chapter 2

Density Functional Theory

The Density Functional Theory is the governing principle behind SIESTA, and it refers primarily to the description of atoms, molecules and solids in their ground states based on the electronic density distribution $n(r)$. It was developed by Kohn and Sham [4] based on the exact ground state theory of Hohenberg and Kohn [5].

Some of the advantages of DFT over other methods worth mentioning are:
1. the higher degree of intuitiveness behind the 3-dimensional electron density when compared to the $3N$-dimensional wave-function,
2. a higher degree of computational simplicity
3. it's ability to handle infinite periodic systems and large (hundreds to thousands of atoms) non-periodic systems.

2.1 Hohenberg-Kohn theorems

The foundation of DFT is based on two theorems first proven by Hohenberg and Kohn:
I. For any system of interacting particles in an external potential $v(r)$, the potential $v(r)$ is determined uniquely, except for a constant, by the ground state electron density $n(r)$.
II. A universal functional for the energy $E(n(r))$ can be defined, valid for any external potential $v(r)$. For any particular $v(r)$, the exact ground state energy of the system is the global minimum value of this functional, and the density $n(r)$ that minimizes the functional is the exact ground state density. [3] [5]
Also Kohn and Sham proposed an *ansatz* that basically rests on the assumption that the exact ground state density can be represented by the ground state density of an auxiliary system of non interacting particles. Although this statement is not at all obvious, the ansatz is now a rigorously established theory.

The first hurdle to pass would be proving the uniqueness of the groundstate electron density $n(r)$ for an interacting N-electron system in an external potential $v(r)$ (for example, the ionic potential). The proof is as follows:
-consider an external potential $v(r)$ with the associated ground state density $n(r)$, the total number of particle $N \quad \int n(r)dr$, Hamiltonian H and ground state and energy ϕ and E :

$$v : H, N, n(r), \phi, E \tag{2.1}$$

-also, consider a second system:

$$v' : H', N, n'(r), \phi', E' \tag{2.2}$$

where $v' \neq v + C$ and hence $\psi' \neq \psi$.

By the Rayleigh Ritz variational principle :

$$E = \langle\phi|H|\phi\rangle \quad < \quad \langle\phi'|H|\phi'\rangle \tag{2.3}$$

and

$$\langle\phi'|H|\phi'\rangle \quad \langle\phi'|H'|\phi'\rangle + \int (v(r) - v'(r))n'(r)dr \tag{2.4}$$

or

$$E < E' + \int (v(r) - v'(r))n'(r)dr \tag{2.5}$$

Since $n'(r) \equiv n(r)$ is excluded because (2.5) would result in $0 < 0$, it can be stated that any potential $v'(r)$ except $v(r) + c$ leads to $n'(r) \not\equiv n(r)$. This means that all properties derivable from H, such as the many electron ground state wave function and the energy can be derived from $n(r)$.

The second theorem is as easily proven:
-consider a system with the ground state electron density $n_1(r)$ that corresponds to the external potential $v_1(r)$, and for these corresponds the expectation value of the Hamiltonian in the ground state

$$E_1 = E[n_1(r)] = \langle\psi_1|H_1|\psi_1\rangle \tag{2.6}$$

-considering a different density $n_2(r)$ that necessarily corresponds to a different wavefunction ψ_2, it fallows that the energy E_2 of this state is greater than E_1

$$E_1 = \langle\psi_1|H_1|\psi_1\rangle < \langle\psi_2|H_1|\psi_2\rangle = E_2 \tag{2.7}$$

2.2 Kohn-Sham equations

Since it has been shown that all we need to know is groundstate electron density, the Kohn-Sham equation can now be introduced. The Kohn-Sham equation is nothing else than a Schrödinger-like equation of a system of non-interacting particles that generates the same electron density as the system of interacting particles. The way Kohn and Sham managed this is by defining a fictitious external potential in which the non-interacting particles move that incorporates all the many-body effects:

$$\left(-\frac{\hbar^2}{2m}\nabla^2 + v_{KS}(r)\right)\phi_i(r) = E_i\phi_i(r) \tag{2.8}$$

The energy can be explicitly written as:

$$E[\psi(\vec{r})] \quad T_e + U_{nn} + U_{ne} + U_{ee} + E_{xc} \tag{2.9}$$

Where:

- U_{nn} is the energy that corresponds to the nucleus-nucleus electrostatic interaction

$$U_{nn} = \frac{1}{2}c_0^2 \sum_{\alpha\neq\beta} \frac{Z_\alpha Z_\beta}{R_{\alpha\beta}} \tag{2.10}$$

- U_{ne} is the total electron potential energy due to the nuclei

$$U_{ne} = \int V_n(\vec{r}) n(\vec{r}) d^3r \tag{2.11}$$

and V_n represents the potential energy of one electron in the electrostatic field of all the nuclei

$$V_n(\vec{r}) = -e_0^2 \sum \frac{Z_\alpha}{|\vec{r} - \vec{R_\alpha}|} \tag{2.12}$$

- U_{ee} represents the Hartree energy, the energy that describes the electrostatic interaction between all the electrons, considered to be stationary

$$U_{ee} = \frac{1}{2} \int V^H(\vec{r}) n(\vec{r}) d^3r \tag{2.13}$$

where $V^H(\vec{r})$ is the energy of one electron at $\vec{r}$ in the field of all the other electrons

$$V^H(\vec{r}) = e_0^2 \int \frac{n(\vec{r'}) d^3r'}{|\vec{r} - \vec{r'}|} \tag{2.14}$$

- $V^H(\vec{r})$ is connected to the charge density $n(\vec{r})$ via Poisson's equation

$$\nabla^2 V^H(\vec{r}) = -4\pi e_0^2 n(\vec{r}) \tag{2.15}$$

- the electron density can be expressed as sum over the wavefunctions

$$n(\vec{r}) = \sum g_i |\psi_i(\vec{r})|^2 \tag{2.16}$$

where g_i is the occupancy of the state

- the wavefunctions $\psi_i(\vec{r})$ are orthonormal solutions to the Kohn-Sham equation and are known as the Kohn-Sham orbitals

$$\int \psi_i^*(\vec{r}) \psi_j(\vec{r}) d^3r = \delta_{ij} \tag{2.17}$$

- we can now express T_e, that represents the kinetic energy, as

$$T_e = \sum_i g_i \int \psi_i^*(\vec{r}) \left(\frac{h^2}{2m} \nabla^2 \psi_i(\vec{r}) \right) d^3r \tag{2.18}$$

- the last term that appears in the energy functional is the exchange-correlation energy

$$E_{xc} = \int \int_{xc}(n(\vec{r}) d^3r \tag{2.19}$$

2.3 Exchange-correlation energy

The exchange correlation energy is the only one of the aforementioned terms that is not exactly known and must be approximated, to a certain extent, by relying on the partial and interpolated results obtained for simpler systems and by taking into consideration either the local value of the electron density (LDA - Local Density Approximation) or by using a more rigorous expression that takes into consideration even the variation of the density (GGA - Generalized Gradient Approximation). Although the exchange-correlation energy might tend to get passed over at first glance because of it's reduced weight when compared to the others, it is found to be of great importance in determining the correct properties of some materials, especially the ones known to be strongly correlated, meaning that the multiparticle effects play an important part. If this exchange-correlation term would be exactly known, the results of DFT could be completely accurate, but since it is strictly an effect due to the multi-particle nature of the material, it's investigation is by no means a simple task, [7]. Because of the importance of the exchange-correlation energy it is worth mentioning a few other details about it.

- E_{xc} can be split up in two separate items, the exchange energy E_x and the correlation energy E_c

$$E_{xc} - E_x \mid E_c \tag{2.20}$$

- the exchange energy is a direct effect of the Pauli exclusion principle that applies to overlapping wavefunctions of indistinguishable particles, and has the expression

$$E_x - -\frac{1}{2}\sum_{ij}\int dr \int dr' \frac{\psi_i^*(\vec{r})\psi_i(\vec{r}')\psi_j^*(\vec{r}')\psi_j(\vec{r})}{|\vec{r}-\vec{r}'|} \tag{2.21}$$

- the correlation energy describes the tendency of electrons to avoid each other because of their Coulomb repulsion; since it depends on both static and dynamic effects, it is harder to calculate. The effect of exchange and correlation can be seen as a bubble or a hole that surrounds electrons that reduces the chance of other electrons being found at the same position [6].

2.4 DFT self-consistent algorithm

We will use the notions above to obtain the Kohn-Sham equations by using the variational principle. By using Lagrange multipliers and taking into account the orthonormality conditions for the wavefunctions ψ_i we end up with the next functional derivative:

$$\frac{\delta}{\delta\psi_i^*(\vec{r})}\left(T_e + U_{nn} + U_{ne} + U_{ee} + E_{xc} - \sum_i \lambda_i \int \psi_i^*(\vec{r})\psi_i(\vec{r})d^3r\right) \quad 0 \tag{2.22}$$

Knowing that the functional derivative is nothing but:

$$\delta F[f(x)] \quad F[f(x)+\delta f(x)] \quad \int \frac{\delta F}{\delta f(x)}\delta f(x)dx \tag{2.23}$$

it is straightforward that:

$$\frac{\delta T_e}{\delta\psi_i^*(\vec{r})} - -g_i\frac{h^2}{2m}\nabla^2\psi_i(\vec{r}) \tag{2.24}$$

$$\frac{\delta U_{ne}}{\delta \psi_i^*(\vec{r})} - g_i V_n(\vec{r})\psi_i(\vec{r}) \tag{2.25}$$

$$\frac{\delta E_{xc}}{\delta \psi_i^*(\vec{r})} \quad g_i f'_{xc}(n(\vec{r}))\psi_i(\vec{r}) \tag{2.26}$$

$$\frac{U_{nn}}{\delta \psi_i^*(\vec{r})} - 0 \tag{2.27}$$

and

$$\frac{\delta}{\delta \psi_i^*(\vec{r})}\left(-\sum_i \lambda_i \int \psi_i^*(\vec{r})\psi_i(\vec{r})d^3r\right) - -\lambda_i \psi i(\vec{r}) \tag{2.28}$$

and, knowing that $\delta U_{ee} - \int \delta V^H \, nd^3r \mid \int V^H \delta n d^3r$ and by using Poisson's equation, after integrating by parts twice, we end up with:

$$\frac{U_{ee}}{\delta \psi_i^*(\vec{r})} - g_i V^H(\vec{r})\psi_i(\vec{r}) \tag{2.29}$$

At last, we find that the Kohn-Sham orbitals must be solutions to the following set of equations:

$$-\frac{h^2}{2m}\nabla^2\psi_i(\vec{r}) + V(\vec{r})\psi_i(\vec{r}) \quad \frac{\lambda_i}{g_i}\psi_i(\vec{r}) \tag{2.30}$$

where $V(\vec{r}) - V_n(\vec{r}) \mid V^H(\vec{r}) \mid f'_{xc}(n(\vec{r})$ is the Kohn-Sham potential. In order to use the Kohn-Sham equations numerically for a certain system, they must be included in a self consistency loop. A possible schematic representation would be the following:

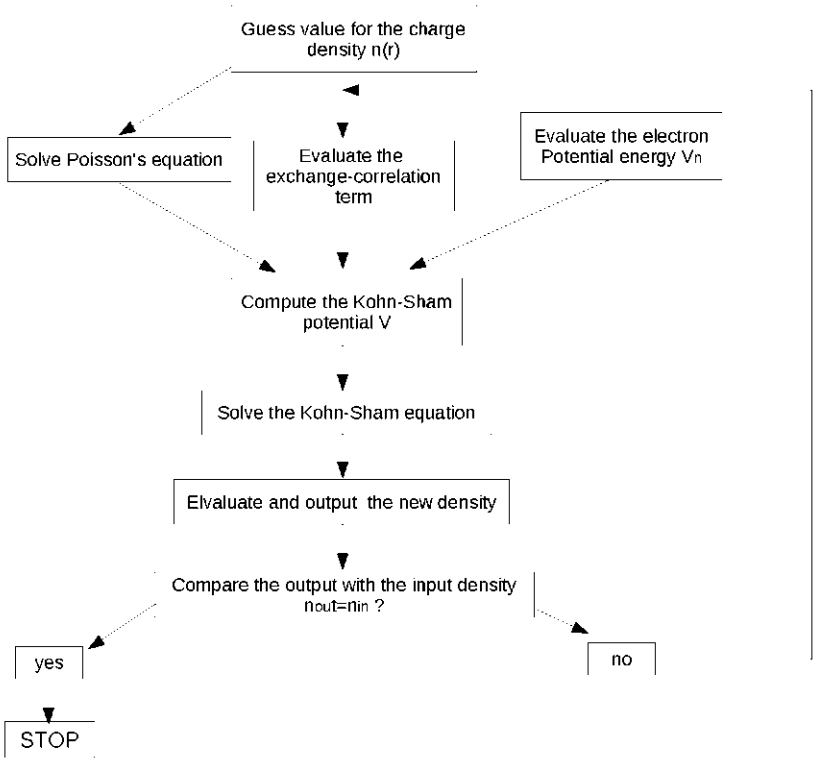

Figure 2.1: DFT self-consistent scheme

After obtaining the full set of solutions, the system's wavefunction, which must be anti-symmetric, can be written as a Slater determinant:

$$\mathbf{\Psi}(r_1, r_2, ..., r_N) - \frac{1}{\sqrt{N!}} \begin{vmatrix} \psi_1(r_1) & ... & \psi_1(r_N) \\ ... & ... & ... \\ \psi_N(r_1) & ... & \psi_N(r_N) \end{vmatrix} \tag{2.31}$$

Chapter 3

Pseudopotentials

3.1 Norm-preserving pseudopotentials

Pseudopotentials are objects that approximate, to an arbitrary degree, a more complex system, for example, they are used here to replace the potential of the core electrons (all electrons that lie on occupied electron shells) and nuclear potential of atoms with a less complicated potential. This method was first introduced by Hans Hellmann in the 1930s [10]. The pseudopotential has the effect of'ironing out' the fast varying nodes of the wavefunction by 'freezing' the core electrons and explicitly dealing only with the chemically active valence electrons i.e. the electrons responsible for the actual chemical bonds. The most important parameter that determines the degree to which the core electrons are approximated is the cutoff radius r_c that determines the actual physical length to which the pseudo-wavefunction $\psi^{ps}(\vec{r})$ is kept identical to real, all electron, wavefunction $\psi^{ae}(\vec{r})$ (wavefunction computed from the all-electron simulation) and is usually positioned about the outermost maximum of the wavefunction . The cutoff radius can be different for different l numbers. This kind of pseudopoptentials are called norm-preserving because:

$$\int_0^{r_c} \psi^{ae*}(\vec{r})\psi^{ae}(\vec{r})dr - \int_0^{r_c} \psi^{ps*}(\vec{r})\psi^{ps}(\vec{r})dr \tag{3.1}$$

The ones with a larger cutting radius r_c are called *softer* (because their pseudo-wavefunction is smoother) and are also less *transferable*, that is, they capture less of the properties of the actual atom and lead to better or, in this case, worse predictions for the energy levels and wavefunctions depending on the surrounding environment they are placed in. *Transferability* can be shown to be related to the existence of a region around the nucleus where the charge density is independent of the chemical environment [12].

3.2 Obtaining the pseudopotentials

The pseudopotentials are obtained in the following way:

- the radial parts of the all electron wave-functions $\psi_l^{ae}(\vec{r})$ and energies E_l^{ae} are obtained from a DFT calculation by solving the radial Kohn-Sham equation (for the non-relativistic case):

$$\left(-\frac{h^2}{2m}\frac{d^2}{dr^2} + \frac{h^2}{2m}\frac{l(l+1)}{r^2} + V(r)\right)\psi_l^{ae}(r) = E_l^{ae}\psi_l^{ae}(r) \tag{3.2}$$

- the pseudo-wave-functions ψ_l^{ps} are generated and the radial Kohn-Sham equation is inverted in order to obtain the screened pseudopotential V_l^{ps}
- the unscreened pseudo-potential $V_l^{psu}(r)$ is obtained by removing the effect of the valence electrons

$$V_l^{psu}(r) - V_l^{ps}(r) - V_H(n^{ps}(r)) - V_{xc}(n^{ps}(r)) \tag{3.3}$$

where n^{ps} is the atomic valence charge density [13].

It can be seen that the form of the pseudopotentials obtained is not local (does not depend only on the distance r) but is semilocal, depending on the distance and the angular coordinates (basically, on the quantum number l). The general requirements that must be take into consideration when constructing pseudopotentials are [14]:

- the pseudo-wavefunction must be smooth (contain no nodes)
- the normalized radial pseudo-wave-function must be equal to the normalized radial all-electron wave-function beyond the chosen cutoff radius
- the charge enclosed within the sphere of radius r_c must be equal for the two wavefunctions
- and the valence all-electron and pseudopotential eigenvalues must be equal

Although the DFT method does not require or imply the use of pseudopotentials, it is obvious that by reducing the number of electrons that are taken into account and thus by reducing the number of basis sets needed for the actual calculation we can achieve a better scaling with time.

The SIESTA package includes a program, entitled Atom, dedicated to obtaining the pseudopotentials that correspond to an atom of theoretically any chemical species (even artificial atoms) and of any energy (even pseudopotentials for excited states are obtainable), with the specific approach used here being that of Troullier and Martins [11] (used to obtain the pseudo-wavefunction) coupled with LDA approximation and the Ceperley-Alder 'flavor' for the expression of the interpolated exchange-correlation energy [9].

3.3 Kleinman-Bylander projectors

A further step is taken in order to optimize the computational side of the problem: instead of using the semi-local form obtained above, a non-local form proposed by Kleinman and Bylander is preferred [15]. By using a non-local form it is possible to split the pseudopotential in a purely long -range local part $V_{local}(r)$ that depends only on the position and is the same for all quantum numbers, and a short range, angular momentum dependent, non-local part $\hat{V}^{KB}$. First of all, a set of orthogonal wavefunctions must be obtained for the non-local pseudopotential, based on the solutions to the radial Kohn-Sham equation for the screened semilocal pseudopotential

$$\left(-\frac{1}{2}\frac{d^2}{dr^2} + \frac{l(l+1)}{2r^2} + V_l^{ps}(r)\right)\psi_{ln}(r) \quad E_{ln}\psi_{ln}(r) \tag{3.4}$$

by using an orthogonalization scheme proposed by Blöchl [16]:

$$\varphi_{ln}(r) \quad \psi_{ln}(r) - \sum_{n'-1}^{n-1} \varphi_{ln'}(r) \frac{\langle \varphi_{ln'} | \delta V_l(r) | \phi_{ln} \rangle}{\langle \varphi_{ln'} | \delta V_l(r) | \varphi_{ln'} \rangle} \tag{3.5}$$

where $\delta V_l(r) \quad V_l^{ps}(r) - V_{local}(r)$. The local pseudopotential $V_{local}(r)$ is arbitrary as long as it joins the semilocal pseudopotential V_l^{ps} beyond the core radius r_{core} . which is the highest valued cutting radius amongst all l: r. and , in the case of the SIESTA method, it is chosen to be as smooth (*transferable*) as possible; as a consequence of Gauss' law. both the local and semilocal pseudopotential become equal to the all-electron potential beyond r_c. It can be seen that the non-local part goes to zero for $r > r_c$.

The Kleinman-Bylander (KB) projection functions are:

$$\chi_{lmn}^{KB}(r) - \delta V_l(r) \varphi_{ln}(r) Y_{lm}(\hat{r}) \tag{3.6}$$

with Y_{lm} being a spherical harmonic function and $\hat{r}$ is the versor $\hat{r} - \frac{\vec{r}}{r}$.
The actual projector is:

$$\hat{V}^{KB} - \sum_{l \ 0}^{l_{max}^{KB}} \sum_{m \ -l}^{l} \sum_{n-1}^{N_l^{KB}} |\chi_{lmn}^{KB}\rangle \ \langle \varphi_{ln} | \delta V_l(r) | \varphi_{ln} \rangle \ \langle \chi_{lmn}^{KB}| \tag{3.7}$$

which leads to the non-local KB pseudopotential:

$$\hat{V}^{PS} \quad V_{local}(r) + \hat{V}^{KB} \tag{3.8}$$

One disadvantage of using the Kleinman-Bylander pseudopotential form is the possibility of producing the so called "ghost states" which have energies close to or below the valence states, and even lower than the first, nodeless, wavefunction; care must be taken to avoid such unwanted states [17].

Chapter 4

SIESTA

4.1 Basis set

The success of the SIESTA method comes from being able to tackle systems with a large number particles, and, implicitly, with a large number (hundreds) of atoms. The way this is made possible is by relying on the sparsity of the Hamiltonian and overlap matrices which is achieved by using a set of strictly localized basis orbitals:

$$H_{ab} - \left\langle \phi_a | \hat{H} | \phi_b \right\rangle - \int \phi_a^*(\vec{r}) \hat{H} \phi_b(\vec{r}) d\vec{r} - 0 \tag{4.1}$$

$$S_{ab} - \langle \phi_a | \phi_b \rangle - \int \phi_a^*(\vec{r}) \phi_b(\vec{r}) d\vec{r} - 0 \tag{4.2}$$

This translates into neglecting the interactions with particles that are far away (more than a couple of lattice constants) which is an acceptable assumption. This numerical LCAO basis set is made out of orbitals that have the form of numerical radial function times a spherical harmonic $\phi_{lmn}(\vec{r}) \quad \phi_{ln}(r_l) Y_{lm}(\hat{r})$ (with: $r_i \quad r - R_i$, R_i being the position of atom i; $r \quad |\vec{r}|$; $\hat{r} \quad \frac{\vec{r}}{r}$) and are obtained by solving the Kohn-Sham equations for an atom inside a confining potential. An important step here is the choice of the actual confinement potential because if it is too hard (varies too abruptly) the orbitals and their derivatives become discontinuous and if it is too soft the basis would have a large spatial extent. The way this problem is dealt with is by choosing a confinement potential :

$$V(r) - V_0 \frac{e^{-\frac{R_c - R_i}{r - R_i}}}{R_c - r} \tag{4.3}$$

where the parameters R_i, R_c and V_0 can be independently adjusted. There are also ways to enlarge the basis, when it is needed, by generating more than one orbital per angular momentum or even generate a polarized orbital in order to better describe orbital hybridization [18]. It should be mentioned that there are no restrictions on the choice of basis set from the method itself, i.e. the user can chose any radial dependent functions whatsoever to serve as basis sets. It must be said that the numerical LCAO basis represents only the real-space part of the Bloch wavefunctions that are used, and that the real-space and k-space integrals are treated separately. [18]

4.2 One-electron Hamiltonian

By using the KB approach, the Kohn-Sham one-electron Hamiltonian can be written as

$$\hat{H} - \hat{T} \mid \sum_i V_i^{local}(r) \mid \sum_i \hat{V}_i^{KB} \mid V^H(r) \mid V^{xc}(r) \tag{4.4}$$

where $\hat{T} - -\frac{1}{2}\nabla^2$ is the kinetic energy operator, i is the atomic index, $V^H(r)$ and V^{xc} are the total Hartree and exchange-correlation potentials and $V_i^{local}(r)$ and $\hat{V}_i^{KB}$ are the local and KB potentials for atom i. In order to counteract the effect of the spatially extended positive local potential V^{local}, a negative screening potential is used. The seeming potential V^{atom} is generated by an atomic density n^{atom} constructed by populating the basis functions with valence atomic charges. Since the basis functions are zero beyond the cutoff radius $R_c - max(R_c^l)$, the screened neutral-atom (NA) potential $V^{NA} - V^{local} \mid V^{atom}$ is also zero beyond R_c. We define $\delta n(r)$ as being the difference between the electron density $n(r)$ that is obtained after a self-consistency loop and the sum of the atomic densities $n^{atom} \quad \sum_{i-0}^{nr.of atoms} n_i^{atom}$ and $\delta V^H(r)$ is the Hartree energy generated by $\delta n(r)$, which integrates to zero over the entire unit cell and is also much smaller than $\rho(r)$. The Hamiltonian can now be rewritten as:

$$H - \hat{T} \mid \sum_i \hat{V}_i^{NA}(r) \mid \delta V^H(r) \mid V^{xc}(r) \tag{4.5}$$

because

$$V^H(\vec{r}) - \int d\vec{r}' \frac{n(\vec{r}')}{|\vec{r} - \vec{r}'|} - \int d\vec{r}' \frac{n^{atom}(\vec{r}'}{|\vec{r} - \vec{r}'|} \mid \int d\vec{r}' \frac{\delta n(\vec{r}')}{|\vec{r} - \vec{r}'} \equiv V^{atom}(\vec{r}) \mid \delta V^H(\vec{r}) \tag{4.6}$$

The matrix elements of the first two terms of the Hamiltonian are computed as integrals in k-space because they represent convolutions that under the Fourier transform turn into a simple product. The matrix elements of the last three terms are evaluated in discrete points on a real space grid of controllable fineness. Also, the Poisson equation is solved by the method of fast-Fourier-transform taking into account the periodically repeated supercell. Although the description of the algorithm was oversimplified for brevity, more details can be found in [18]. The next step consists of solving the general eigenvalue problem:

$$(H_{N\times N})\,(C_{N\times 1}) - E_{nk}\,(S_{N\times N})\,(C_{N\times 1}) \tag{4.7}$$

where $C_{N\times N}$ are the coefficients of the wavefunction expressed in terms of the localized orbitals.

4.3 Brillouin zone sampling

In order for SIESTA to be able to work successfully for both large unit cells (where a computation in the Γ point can be a sufficiently good approximation) and for smaller unit cells (of a few unit cell lengths in on one or more directions), an auxiliary supercell is defined that is large enough to contain all the atoms from the surrounding cells and from the unit cell itself whose wavefunctions overlap, in any of the real-space grid's points, with

the wavefunctions of the atoms from the unit cell.

The Hamiltonian matrix elements are calculated by summing the integrals for the non-local pseudopotential with the local pseudopotential real-space grid integrals (computed only within the unit cell) between the orbitals in the supercell. The overlap values between the basis orbitals that are computed in every point of the real space grid are than summed up in the corresponding matrix elements. The k-space is treated in similar fashion to the real space, in that the integrals are computed by summing the values from a set of points on a mesh. The k-space mesh can be chosen either as a spherically-symmetric radial grid or a rectangular grid as the one proposed by Monkhorst and Pack [20], taking into account time reversal symmetry by using only half of the Brillouin zone but without making use of the symmetry of the cell.

After the real space overlap and Hamiltonian matrix elements are computed they are multiplied at every k-point by the corresponding phase factors and then summed up by folding the supercell orbitals to their unit-cell counterparts. The resulting $N \times N$ complex eigenvalue problem in solved for each k point, finding the Bloch-state expansion coefficients $c_{ij}(k)$:

$$\psi_i(k,r) \quad \sum_j e^{ikR_j}\phi_j(r)c_{ij}(k) \tag{4.8}$$

Thus, the electron density becomes

$$n(r) - \sum_i \int_{BZ} g_i(k)|\psi_i(k,r)|^2 dk - \sum_{\mu\nu} \rho_{\mu\nu}\phi^*_\mu(r)\phi_\nu(r) \tag{4.9}$$

with the density matrix

$$\rho_{\mu\nu} \quad \sum_i \int_{BZ} c_{\mu i}(k)g_i(k)c_{i\nu}e^{ik(R_\nu - R_\mu}dk \tag{4.10}$$

In the case of 1-D structures, a parallelipipedic supercell is considered, which contains a transverse slice of the nanowires and nanotubes to be investigated. Therefore, the only relevant direction in the Brillouin zone is the Γ-A direction, which corresponds to the longitudinal orientation of the structure.

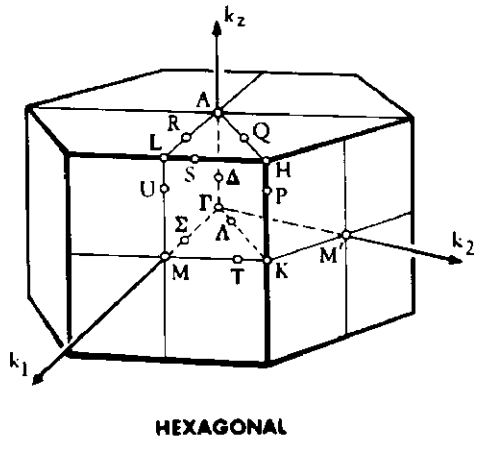

Figure 4.1: Brillouin zone for the hexagonal lattice showing the high symmetry points

4.4 Atomic forces and structure relaxation

Because the atomic coordinates used in the input data do not usually correspond to the real structure, a molecular dynamics self consistent cycle is used for the relaxation of the lattice. SIESTA uses a classical Born-Oppenheimer molecular dynamics method that computes the forces for each ion while ignoring the electronic degrees of freedom, as opposed to the more precise but more computationally expensive Car-Parinello method.

The approximation proposed by Born and Oppenheimer [22] is important because it allows the treatment of systems with quite a large number of atoms (which would be nearly impossible if the nuclear degrees of freedom would be considered). This is done by splitting the wavefunction into an electronic and a separate nuclear component that incorporates the vibrations and rotations of the lattice. Such an approximation is possible only because electrons and ions/nuclei evolve on very different time scales, which is mainly due to the high ratio between nuclear and electron masses, i.e. the motion of the nuclei is perceived by the electrons only as a small perturbation. In essence, electrons only "feel" the clamped (frozen) ionic configuration while the nuclei/ions only "feel" the averaged electron field ([23] - page 93).

The force that acts on each ion, in the case of a clamped ion Hamiltonian (the nuclei and their adjacent core electrons have a fixed position), is computed by making use of the Hellmann-Feynman theorem [21] that states that the force that acts on ion i along the direction j is

$$F_{R_{ij}} \quad -\frac{\partial E^{KS}}{\partial R_{ij}} \tag{4.11}$$

which is none other than

$$-\frac{\partial E^{KS}}{\partial R_{ij}} - - \int \psi^*(R_i, ...)\frac{\partial \hat{H}}{\partial R_{ij}}\psi(R_i, ...)dv \tag{4.12}$$

where "..." represent other parameters that the wavefunction depends on and dv represents the entire domain of the wavefunction. This is true only for a system that lies in a steady state because for a system in a non-steady state the concept of force does not have a clear definition.

A conjugate-gradient method is used to solve the resulting system of equations. After computing the forces for all the atoms and displacing the ions accordingly, a self-consistent cycle is used to obtain the energies and wavefunctions, and subsequently, the forces for the new configuration. Relaxation steps are carried out until a prespecified maximum force tolerance is reached for all of the ions. SIESTA allows users to select between a relaxation that keeps the unit cell fixed and a more precise type of relaxation that also changes the unit cell and, implicitly, the k-space associated to the crystal/structure.

4.5 Phonons

In order to obtain the phonon spectrum for a structure or material, SIESTA must first compute the force-constants matrix. This can be done by a finite difference method that basically consists in moving each atom, by a controllable distance, on all three axes, one by one, both in the positive and negative directions, and running a self consistent loop at each displacement in order to compute the accurate shift in energy, and implicitly,

the force that acts between any two atoms.

After this step, a program entitled Vibra, also part of in the SIESTA package, is used to generate and diagonalize the dynamic matrix in order to obtain the phonon frequency dispersion, in cm^{-1} for each k point. The dynamic matrix is nothing else than the set of equations of motion written in a particular matrix form whose eigenvalues represent the squares of the normal frequency modes and the eigenvectors are the amplitudes of each normal mode.

4.6 Surfaces

Because the systems considered in this work have a large part of their atoms exposed on the surface that separates the material from the surrounding vacuum, their properties become significantly different form their bulk counterpart. The presence of the surface breaks the translational invariance found in the normal bulk material and gives rise to a supplementary confinement potential similar to a (cylindrical) potential well. Another difference represents the rearrangement of atoms on the surface, when compared to the expected bulk positions.

What is generally expected from such structures is the emergence of new type of states, caused exclusively by the changes induced by the surface, which are called surface states, with energies that can lie either in the bandgap or in valence band or conduction band of the normal bulk material [26]. This change brings into the spotlight interesting properties of materials that would have been otherwise ignored [24] [25].

An interesting piece of information is the physical localization of such states because in the case of q-1 D structures the wavefunction may either: lie in its "bulk" (confined inside the structure and not extending to and beyond its surface); or they can be localized on the surface (the first few layers of the surface and even into the near space around the structure), in this case they are known as surface states; or they can be mixed surface and "bulk" states. Surface states are usually caused by spatially extended orbitals like sp^3 or d that stick out of the surface while experiencing significant shifts from the bulk values.

In this work, an approach proposed by García-Gil et al. [27] is used to extend the otherwise localized basis into the surrounding vacuum. This is accomplished by placing a set of "floating orbitals" or "ghost orbitals" (called this way because they are not occupied by extra electrons and do not have an attached ion) in the near vicinity of the surface atoms. García-Gil et al. who have treated the case of infinite 2D slabs and have placed the "ghost orbitals" in positions that would have corresponded to normal bulk-lattice atoms, because the relaxation of the lattice was negligible; in the case of q-1D structures, the lattice relaxation is far greater and placing "ghost orbitals" in the same way would be inadvisable. By using the Hellmann-Feynman method for lattice relaxation, forces can only be computed for ions and not for electrons, and the "ghost orbitals" would remain still during the lattice relaxation and would not follow the lattice atoms. In order to overcome this problem in an systematic way (not by placing the "ghost orbitals" by hand, in an arbitrary fashion) a small program was used to read the positions of the atoms from the previously relaxed nanowires/nanotubes and to place a "ghost" along the radius determined by the center of the wire/tube and each of the atoms of the surface (for both the inside and outside surfaces in the case of tubes). In this manner, a sufficiently uniform "ghost orbital" envelope was generated.

Chapter 5

Results

5.1 The system and computational setup

The first step consisted of obtaining a set of usable pseudopotentials for both boron and nitrogen. The next step that was undertaken consisted of editing the atomic positions of the supercells that correspond to the different structures. In the cases presented here, the purpose was to obtain the properties of isolated nanotubes and nanowires and because of the Born-von Karman periodicity conditions that this method uses, special conditions were required: a large supercell was chosen (a square with a 20 lattice constants long (5.1 nm) side for all the structures except the 5 nm diameter tube for which a 30 lattice constants long side was used (7.65 nm)) in order to minimize the lateral interactions between the structures.

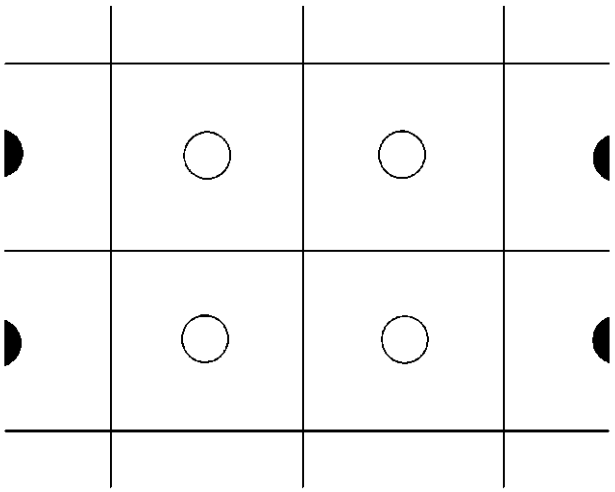

Figure 5.1: Horizontal (xOy) section through a set of adjacent supercells

On the vertical |001| direction, the cylindrical supercell directly joins the adjacent cells and the interactions with these neighboring cells is taken into account.

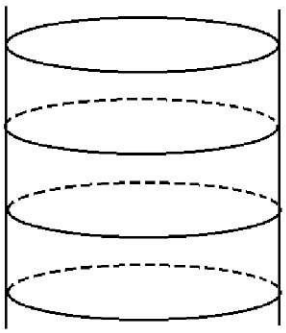

Figure 5.2: Vertical stacking of supercells

Because of the large number of atoms involved, the positions of the atoms in a supercell were determined with the help of a custom editing program that calculated the positions corresponding to a the atoms from a cylindrical section of bulk würtzite BN. In the case of the graphene-like tubes, the atomic positions correspond to the atoms from a rolled-up hexagonal single-layered sheet of two different chiralities (zig-zag and armchair).

Because the atomic positions used were only geometrical estimates of the real positions, a molecular dynamics cycle (see: Atomic forces and structural relaxation) had to be used to determine the atomic positions of the relaxed structures. After the structural relaxation, atoms close to the surface were the ones to change position most significantly, as was expected, and a shift of the N atoms towards the surface of the tube was visible. The würtzite bulk and q-1D structures and the graphene-like tubes were relaxed with a force tolerance of less than 0.01 eV/Ang, but the higher diameter tube (5 nm) only reached a tolerance of approximately 0.04 eV/Ang because of the time computational constraints involved.

A special remark about the molecular dynamics relaxation process is that, although the R = 5 nm, r = 3.6 nm nanotube structure had it's atoms initially positioned in a würtzite arrangement, it clearly switched from the würtzite to a somewhat complex, double-sheet graphene-like structure (Fig.5.3), as opposed to all the others that maintained their general initial structure during the entire lattice relaxation process.

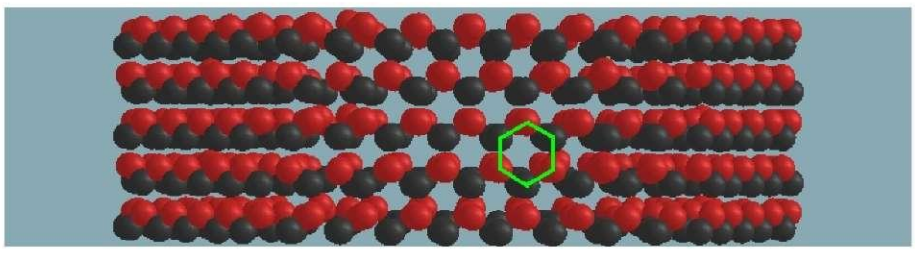

Figure 5.3: Lateral view of the nanotube with 5 nm diameter clearly showing a zig-zag hexagonal graphene-like structure

In the case of the extended surface structure, the atomic positions used where directly those of the final, relaxed structure.

The investigation of the energy dispersion and density of states (DOS) was carried out for each structure and compared to those of the bulk case. For three of the structures more detailed investigation were carried out by plotting out some of the wavefunctions and also by spatially extending the basis in the surface region.

A separate step was undertaken in order to observe the phonon dispersion in some of the structures. Because this type of computation are rather time-demanding only some of the simpler structures were analyzed.

5.2 Pseudopotentials

For both nitrogen and boron, the pseudopotentials were generated with the Ceperley-Adler scheme, the LDA exchange-correlation approach and without considering relativistic effects.

In the case of boron the $1s$ orbital was included in the ionic core, the $2s$ orbital was populated with two electrons and the $2p$ orbital with one electron; for all orbitals the cutting radius r_c was chosen 1.71 Bohrs.

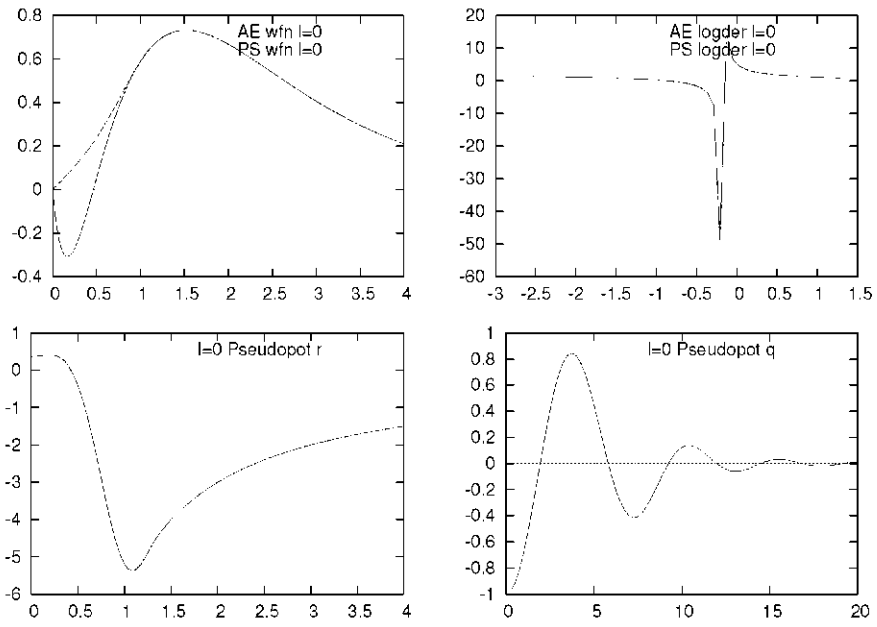

Figure 5.4: Boron s type orbitals: (top left) all electron wavefunction and pseudo-wavefunction; (top right) the logarithmic derivative of the wavefunctions; (bottom left) the pseudopotential; (bottom right) the Fourier transform of the pseudopotential

The images depicting the pseudopotentials also include additional information like: the all electron and pseudo-wavefunction which must be identical beyond r_c and their logarithmic derivatives that point out any unphysical discontinuities; the Fourier transform of the pseudopotential which is important if the potential is expressed as a Fourier series for certain computations.

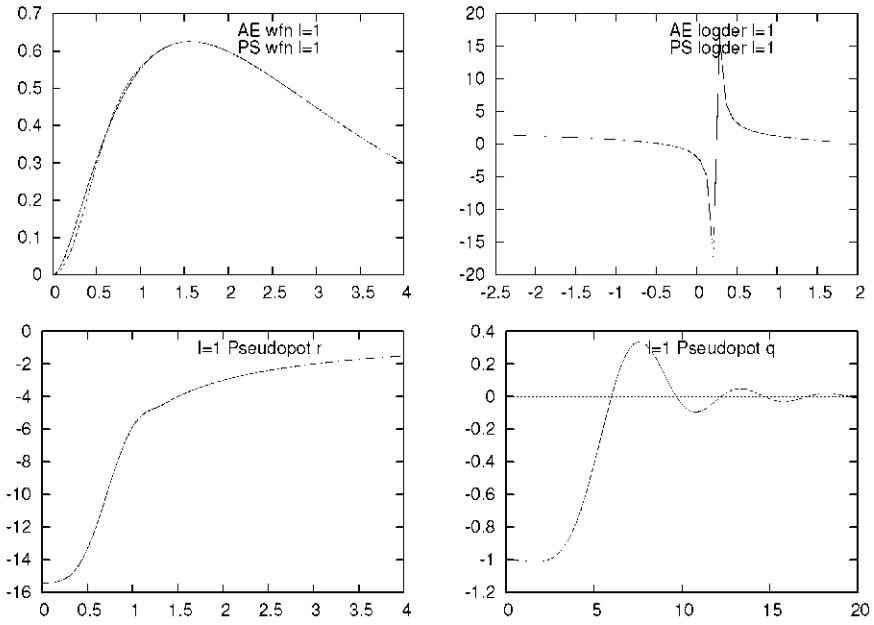

Figure 5.5: Boron p type orbitals: (top left) all electron wavefunction and pseudowavefunction; (top right) the logarithmic derivative of the wavefunctions - shows the discontinuity at r_c; (bottom left) the pseudopotential; (bottom right) the Fourier transform of the pseudopotential

For nitrogen, the $1s$ orbital is again included in the ionic core, the $2p$ orbital is populated with two electrons and the $2p$ orbital is populated with three electrons; for all orbitals the cutting radius r_c was chosen 1.45 Bohrs.

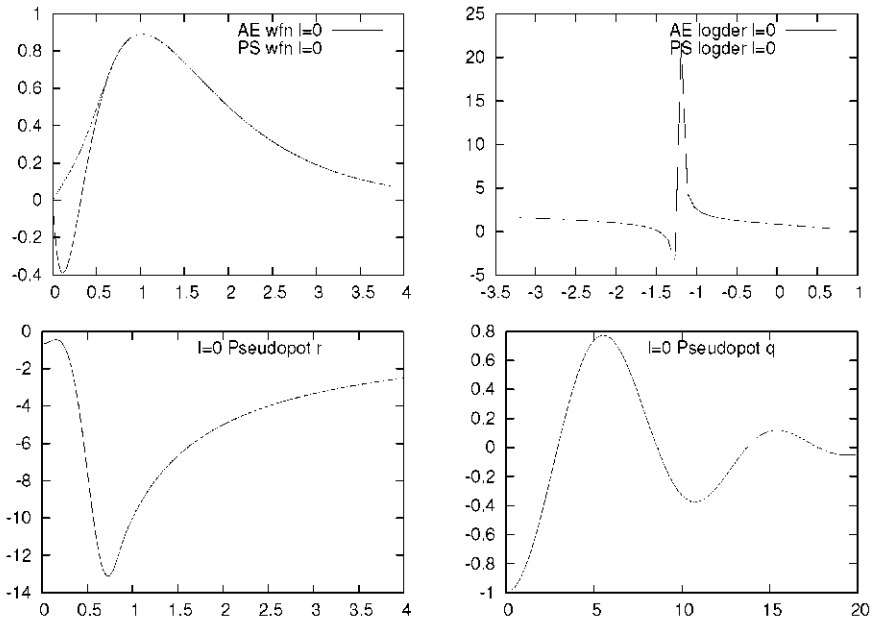

Figure 5.6: Nitrogen s type orbitals: (top left) all electron wavefunction and pseudowavefunction; (top right) the logarithmic derivative of the wavefunctions - shows the discontinuity at r_c; (bottom left) the pseudopotential; (bottom right) the Fourier transform of the pseudopotential

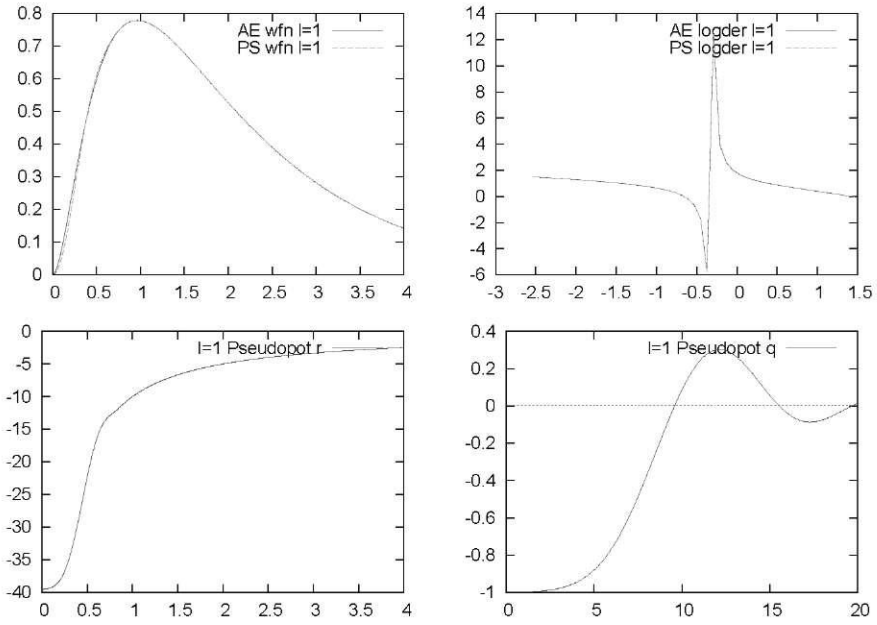

Figure 5.7: Nitrogen p type orbitals: (top left) all electron wavefunction and pseudowavefunction; (top right) the logarithmic derivative of the wavefunctions - shows the discontinuity at r_c; (bottom left) the pseudopotential; (bottom right) the Fourier transform of the pseudopotential

5.3 Band structure DOS for bulk BN

Boron nitride (BN) is a wide band-gap semiconductor (5.05 eV - amorphous, 5.2 eV - hexagonal, 4.5-5.5 eV würtzite, 5.5 eV - diamond) [29] [30]. BN is not found in nature and amorphous-BN is produced synthetically from boric acid or boron trioxide. Alternate methods of preparation or subsequent treatment is required in order convert the amorphous form into others; for example, hexagonal BN is obtained by reacting boron trioxide or boric acid with ammonia or urea in a nitrogen atmosphere, and würtzite BN is obtained by high-pressure or by dynamic shock methods.

It must be mentioned that only graphene-like BN nanotubes have been synthesized and that no records of würtzite BN nanowires or nanotubes currently exist.

For the confirmation of the pseudopotentials' transferability, the energy dispersion and density of states (DOS) have been plotted out for the bulk material (Fig.5.8) of würtzite structure (Fig.5.9). The band structure is in agreement with that obtained by other *ab initio* calculations [28] and the bandgap value is also close to those measured experimentally: 5.9 eV, obtained here, as compared to the measured values of 5.5 eV [29] [30].

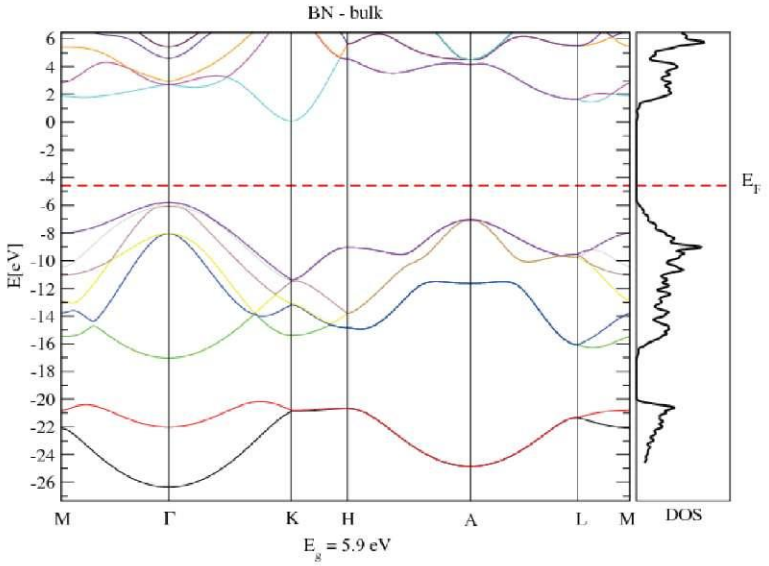

Figure 5.8: Band structure and density of states for bulk BN

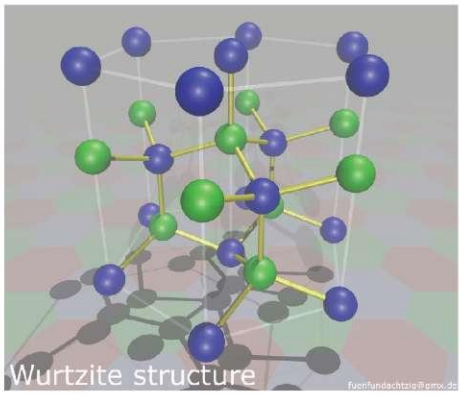

Figure 5.9: Atomic structure of würtzite BN crystal

Because for the q-1D structures the periodicity is maintained only in the Γ-A direction and in order to easily detect the differences in band structure between the bulk material and the q-1D structures, the energy dispersion relation was mapped out for the Γ-A direction in the bulk material (see Fig. 5.10). It must be specified that the DOS corresponding to the conduction band appears to be overhanging beyond the last represented state, but that is the contribution from k-states that are not visible in the Γ-A representation but that can be seen in the vicinity of the K point (Fig.5.8).

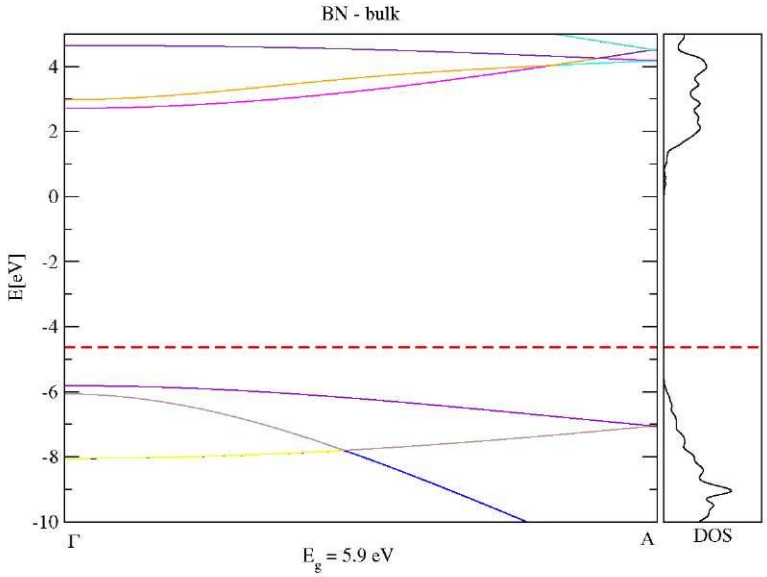

Figure 5.10: Band structure and density of states for bulk BN between Γ and A points

5.4 Band structure, DOS and plotted wavefuntions for the q-1D structures

In order to associate the data to the corresponding structure in a more straightforward manner and in order to avoid repeating the representations of the unrelaxed and relaxed nanowires/nanotubes in a separate section of this chapter, images with sections of the nanotubes and nanowires, both before and after relaxation, are placed next to the graphs.

For all band structure and DOS investigations the structural relaxation was carried out in multiple steps in order to ensure the accuracy of the final results; this is done by comparing the band structures for two successive relaxation steps until no important changes arise.

As a general notation, 'R' stands for the outer radius and 'r' stands for the internal radius of the tube.

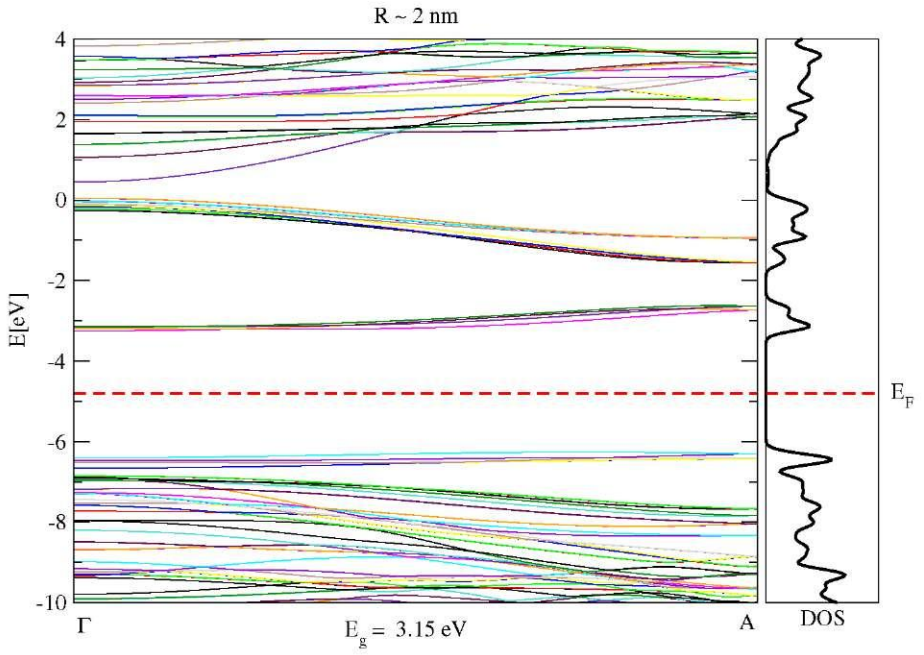

Figure 5.11: Band structure and DOS for the nanowire with R = 2 nm, r = 0 nm

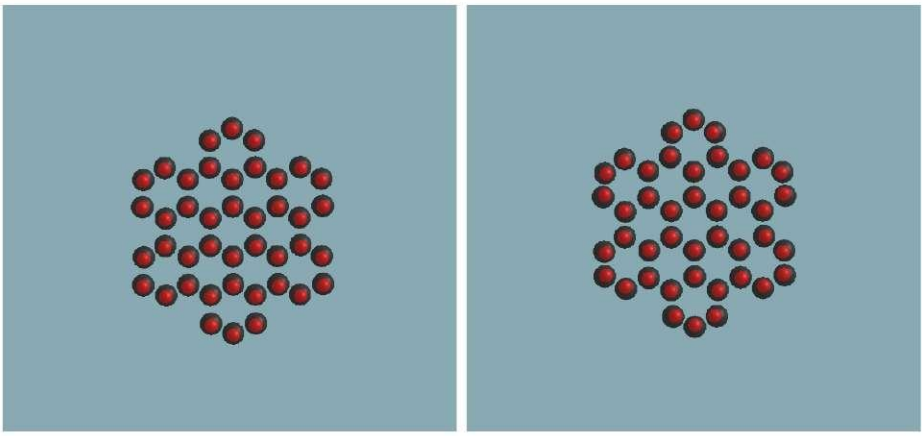

Figure 5.12: Input positions and relaxed, output positions for the nanowire with R = 2 nm (boron in red and nitrogen in blue)

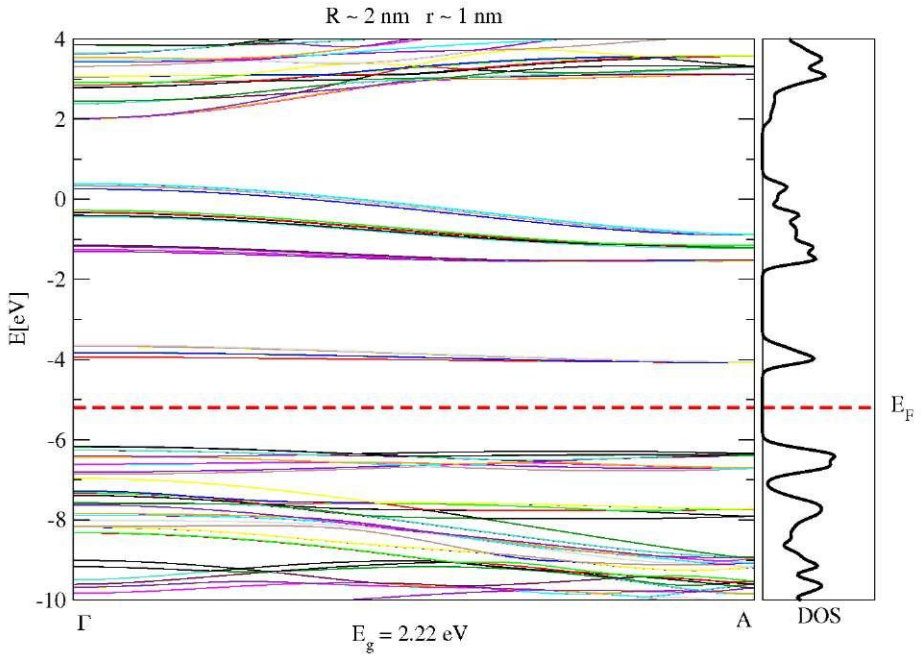

Figure 5.13: Band structure and DOS for the nanowire with R = 2 nm, r = 1 nm

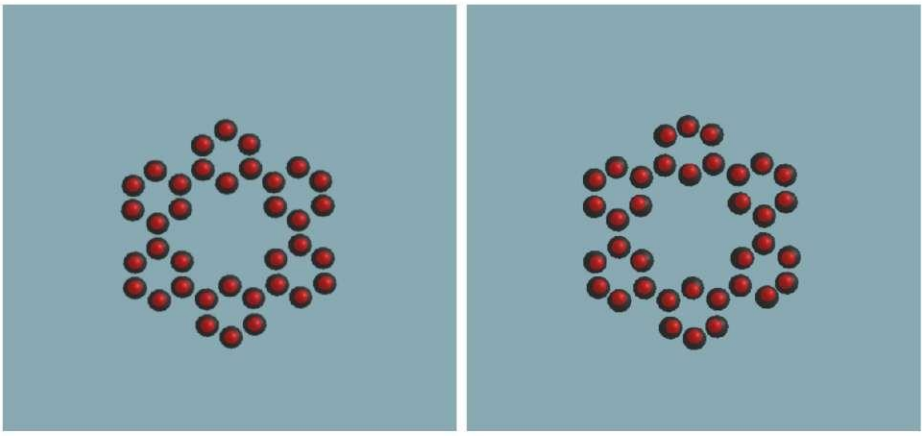

Figure 5.14: Input positions and relaxed, output positions for the nanotube with R = 2 nm and r = 1 nm

The changes in energy dispersion in the new structures is clearly visible: in the case of the nanowire new states appear (Fig.5.11) in the bandgap region from the bulk material as a consequence of the dangling bonds present on the surface. Although the difference is subtle, it can be seen that the secondary interior surface present in the nanotube gives rise to even more states in the bandgap region (Fig.5.13) than in the case of the nanowire; this is also visible as an increase in the density of states in the bandgap region of the nanotube. The first bands below and above the Fermi energy level, which could be considered the new valence and respectively conduction band, are both convex, and could give rise van Hove singularities in the optical spectrum, if the transitions between them are indeed allowed. Another detail worth mentioning is the negative descent of some of the new bands, which give rise to negative electron masses. The lattice relaxation process leads to small position changes for the outermost atoms and displaces the boron atoms inward; these observations are valid for all würtzite structure mentioned in this work.

For the next three cases, a more detailed investigation is carried out by using both the simple and the spatially extended basis. For some of the examples, a number of selected wavefunctions (the absolute value squared) are plotted in an isosurface representation in order to show different types of spatial localization in the new structures; if not mentioned otherwise, the value used for the isosurface represents a 0.5% probability of localization, a value which was chosen low enough to discern some spatial distribution but high enough in order to represent the area of high probability of localization. An important note is that all the following statements are to be considered valid only for the wavefunctions with energies located in the bulk bandgap interval. The isosurface of the charge density is also plotted for a specific value of $1[e_0/A^3]$ (where e_0 stands for the elementary charge) that gives the best visual image while highlighting the high charge density areas.

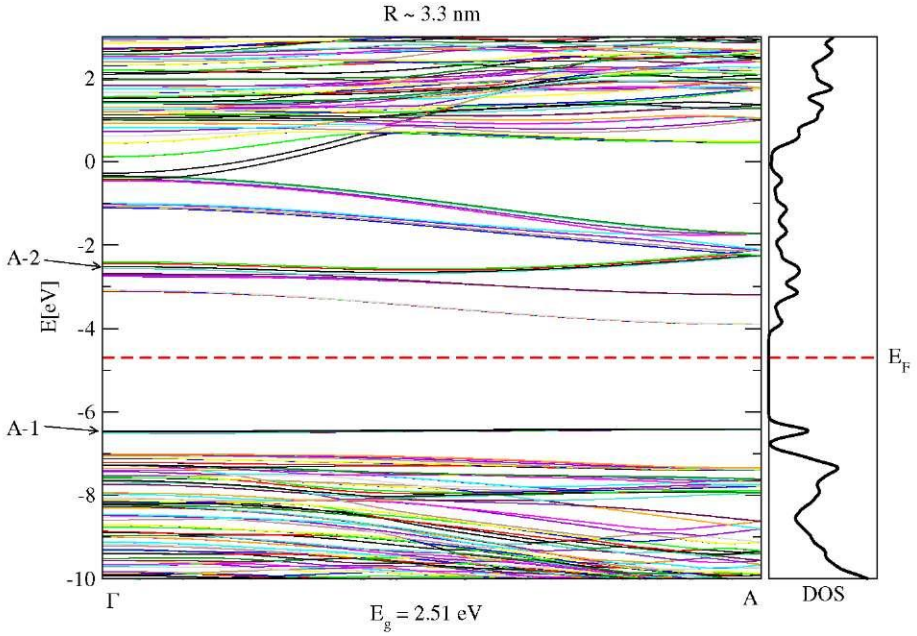

Figure 5.15: Band structure and DOS for the R = 3.3 nm nanowire

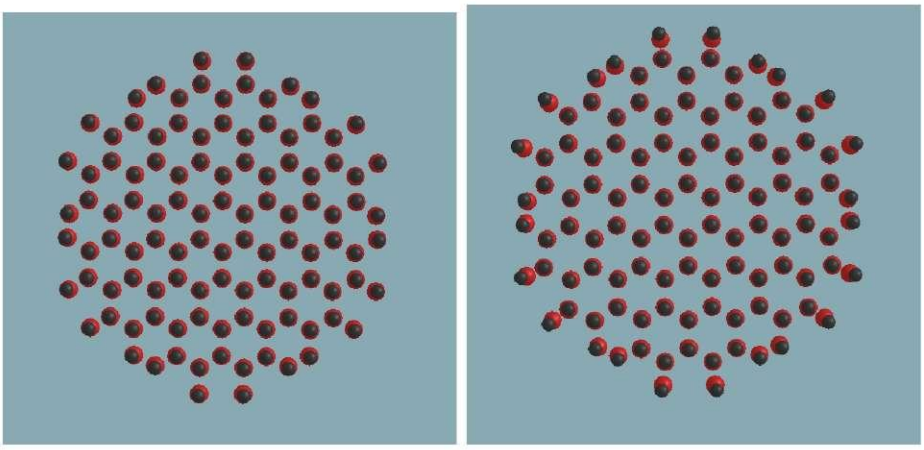

Figure 5.16: Initial and relaxed structure of the R = 3.3 nm nanowire

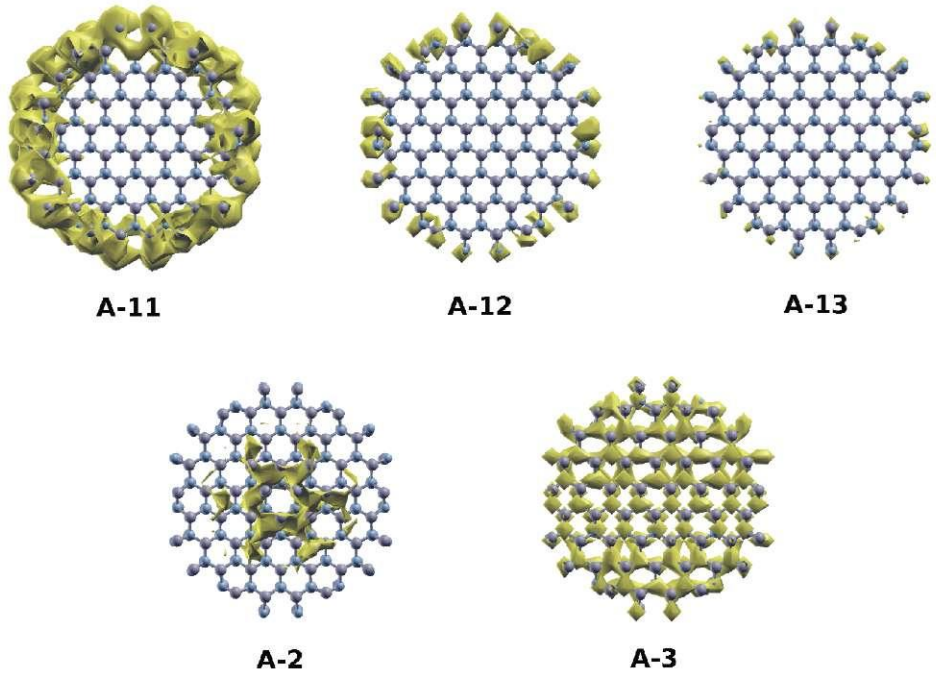

Figure 5.17: Surface localized wavefuntion plotted for thee different values of isosurfaces: A-11 - 2%, A-12 - 5%, A-13 - 8%. Wavefunction localized inside the nanowire - A-2. Charge density plot - A-3.

For the case of the R = 3.3 nm nanotube, the presence of surface states again leads to the appearance of a set of new states in the bulk bandgap (Fig. 5.15). As far as it was possible to determine, given the large number of individual states that are present and taking into account that only a fraction of them were spatially plotted, these new states all appear to be localized on the surface, similar to what can be seen in Fig. 5.17.

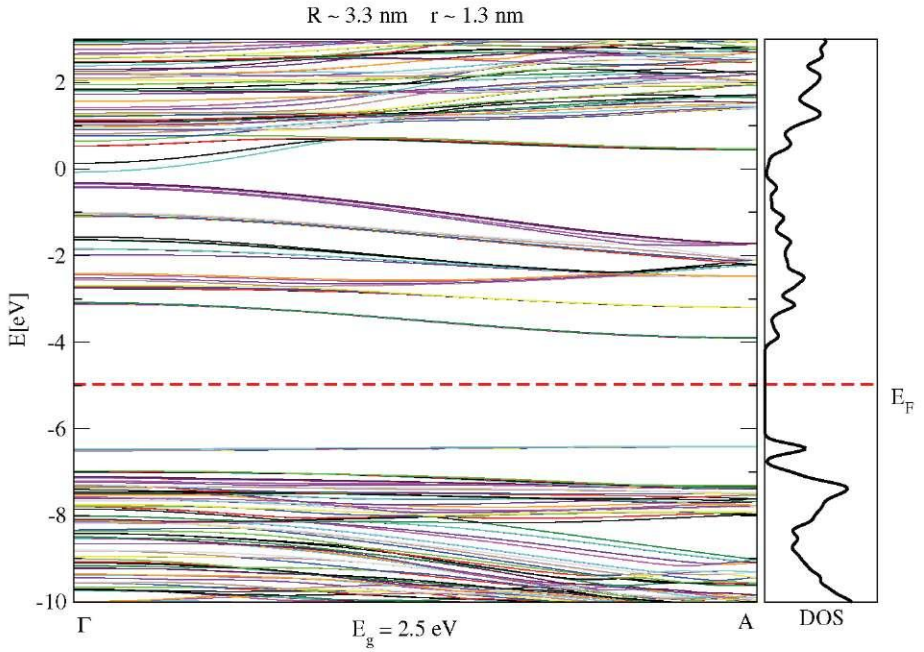

Figure 5.18: Band structure and DOS for the R = 3.3 nm, r = 1.3 nm nanotube

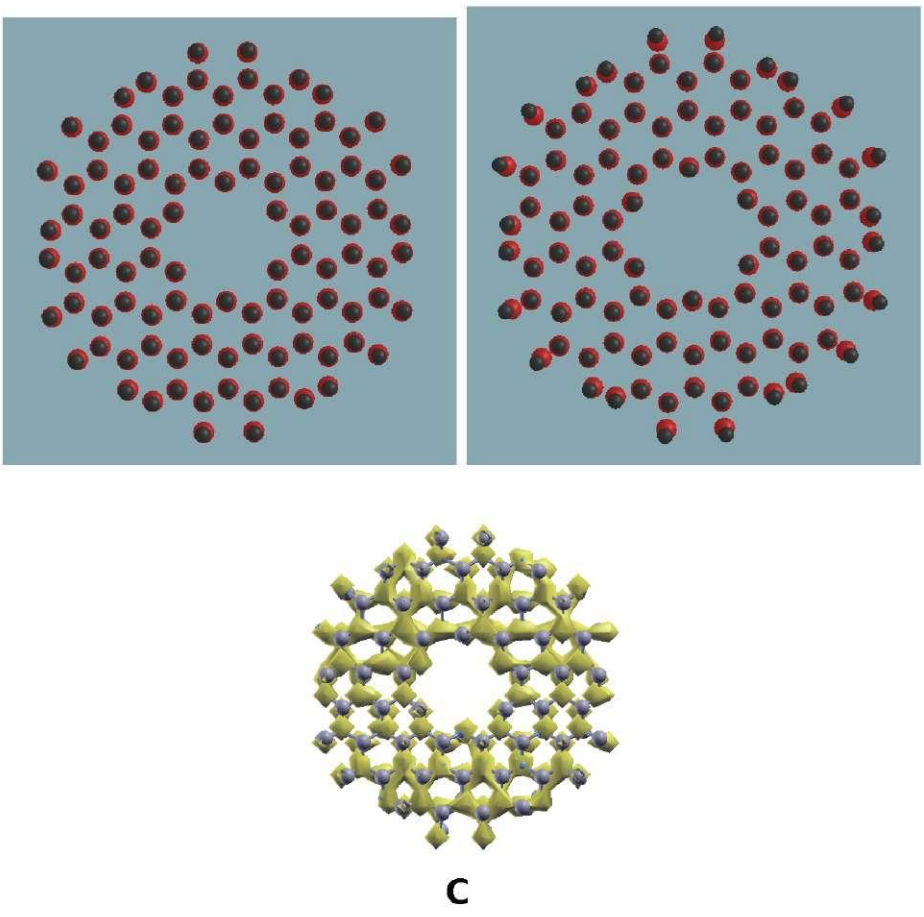

Figure 5.19: The unrelaxed and relaxed atomic position and the charge density distribution (C) for the R = 3.3 nm, r = 1.3 nm nanotube

In the band structure of this new tubular structure (Fig.5.19) an increase in the number of states present in the bandgap and in their corresponding DOS is visible (Fig.5.18) when compared to the nanowire with R = 3.3 nm at Fig.5.16. It is important to notice that the new internal surface does not disrupt the surface states that appeared in the case of the nanowire; it is worth mentioning that, as far as it was investigated, none of the new states that appear in the [-2,-1] eV interval are clearly located on the interior surface which could be explained by the fact that, even though some of the bonds of the atoms located on this secondary surface are left dangling, the interaction with diametrically opposed Coulomb tail of the pseudopotentials is strong enough in order to shift the energy of any states located in this area outside the bandap range of energies; a direct contribution to this effect is the relatively small spatial volume that a state located on the surface would occupy, leading to it having a higher energy than a state that would be located on the larger exterior surface.

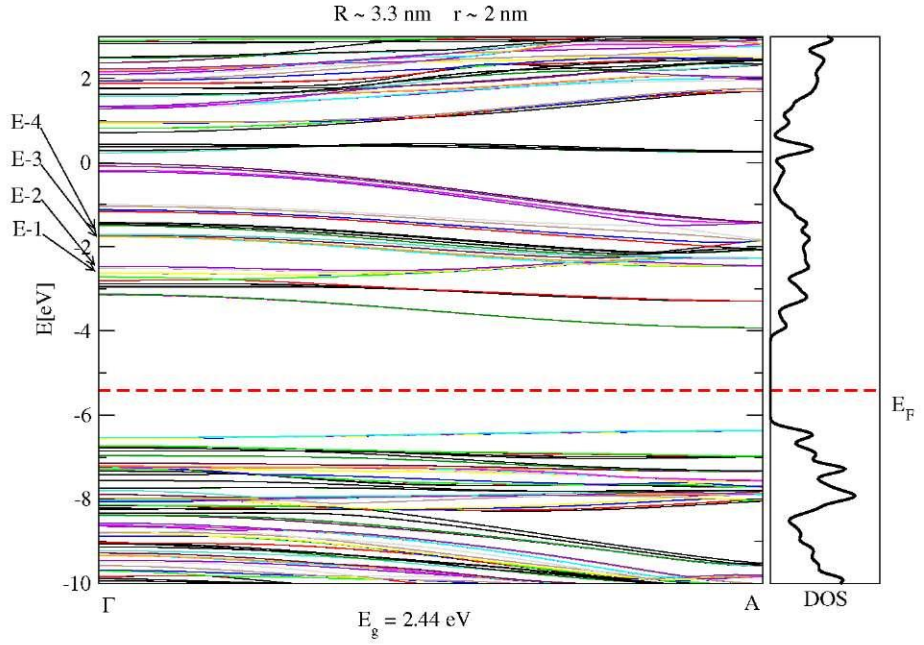

Figure 5.20: Band structure and DOS for the R = 3.3 nm, r = 2 nm nanotube

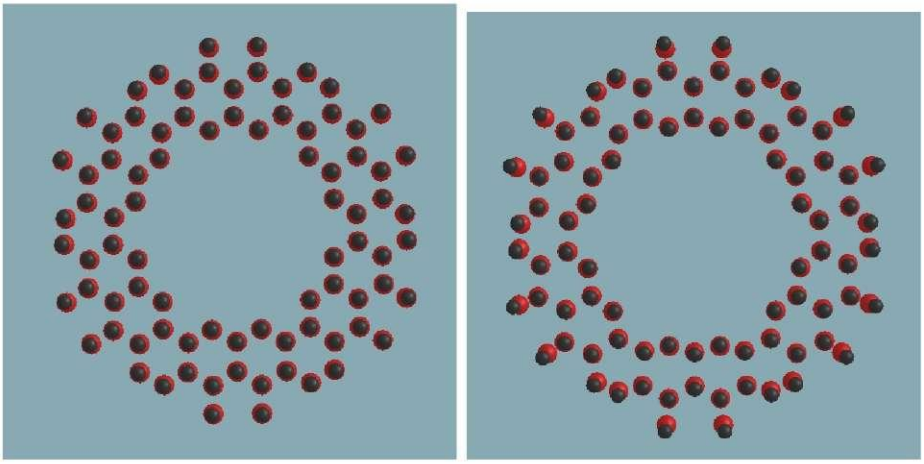

Figure 5.21: The unrelaxed and relaxed atomic position for the R = 3.3 nm, r = 1.3 nm nanotube

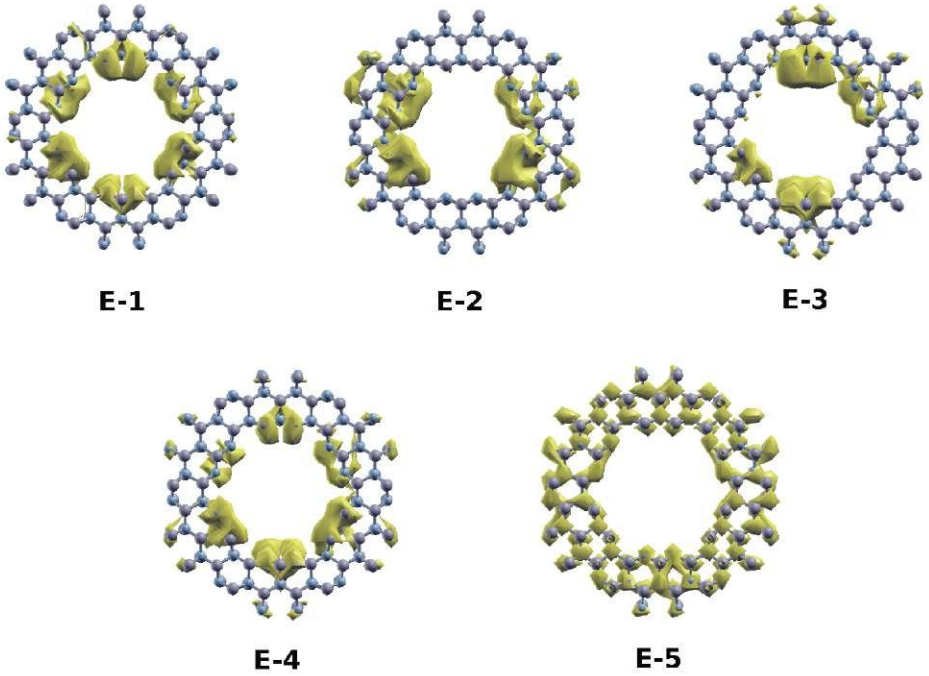

Figure 5.22: Examples of states localized on the interior surface E-1 to E-4 pointed out in Fig.5.20 and charge density distribution E-5.

In the case of the R = 3.3 nm and r = 2 nm nanotube (Fig.5.21) an even higher number of states are present in the bulk bandgap that lead to a higher DOS for the gap energy interval. As in the case immediately above, the surface states that were present in the case of the R = 3.3 nm nanowire are not drastically modified and only suffer a small energy shift. An important difference is that, in this case, states can be found on the interior surface because of a weaker interaction with the Coulomb tail of the opposed ions and a larger localization volume. Another interesting fact that was observed is a modulation of the spatial localization of the surface waves, for both interior and exterior surfaces, that can have two, four or six maxima (Fig5.22). What is also obvious now is the rising of states from the valence band that bunch up in the [-8.2,-6] eV interval.

As mentioned in section 4.6, three of the structures have also been endowed with a "more complete" basis (Fig.5.24, Fig.5.26, Fig5.28) that should lead to a better treatment of the presence surfaces. Although some differences are visible between results of the normal and extended basis band structures (Fig5.23, Fig.5.25, Fig.5.27), they are not so dramatic; that is because of both B and N being light atoms, with very well localized orbitals. However, it is believed that this treatment of surfaces would be much better suited in the case of materials with delocalized d and f orbitals.

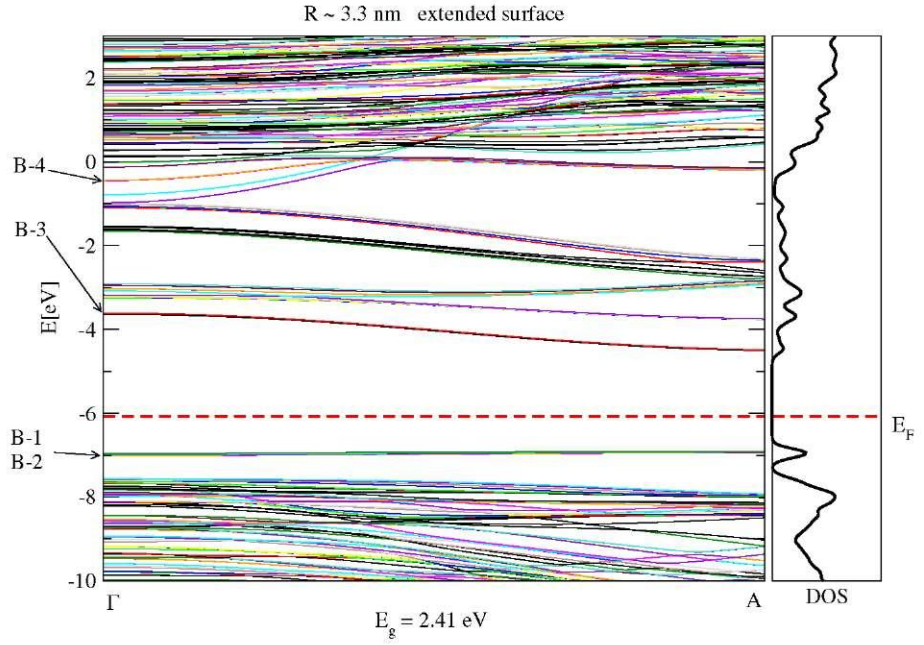

Figure 5.23: Band structure and DOS for the R = 3.3 nm nanowire endowed with a surface extended basis

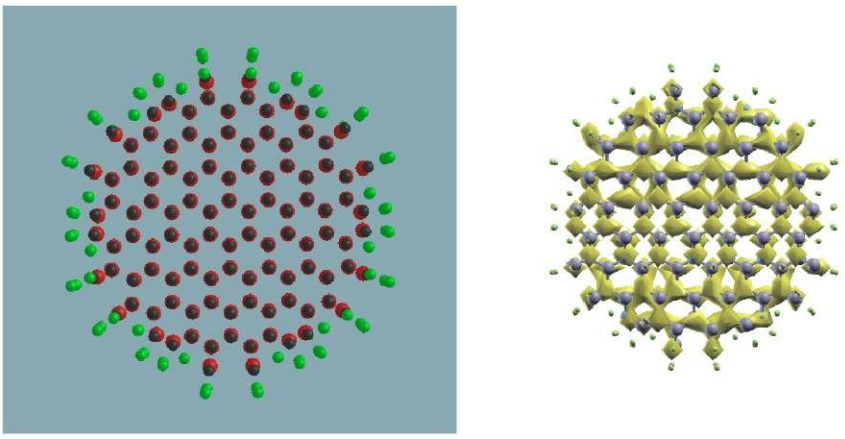

Figure 5.24: Atomic positions and locations of the additional surface extended basis (in green) and charge density distribution for the R = 3.3 nm nanowire

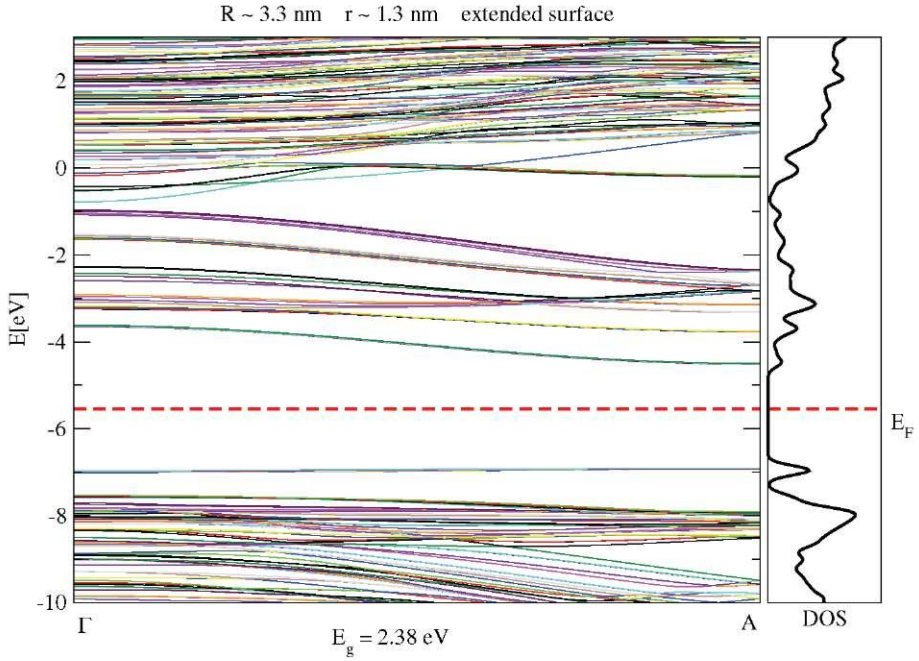

Figure 5.25: Band structure and DOS for the R = 3.3 nm, r = 1.3 nm nanotube endowed with a surface extended basis

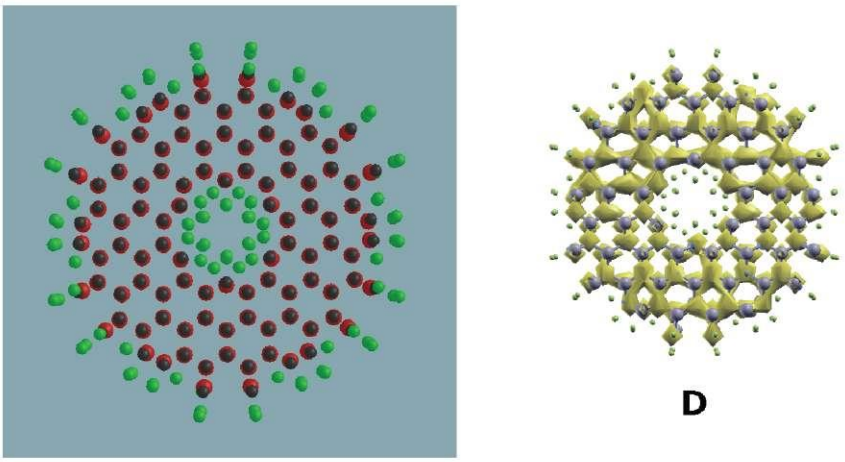

Figure 5.26: Atomic positions and locations of the additional surface extended basis (in green) and charge density distribution for the R = 3.3 nm r = 1.3 nm nanotube

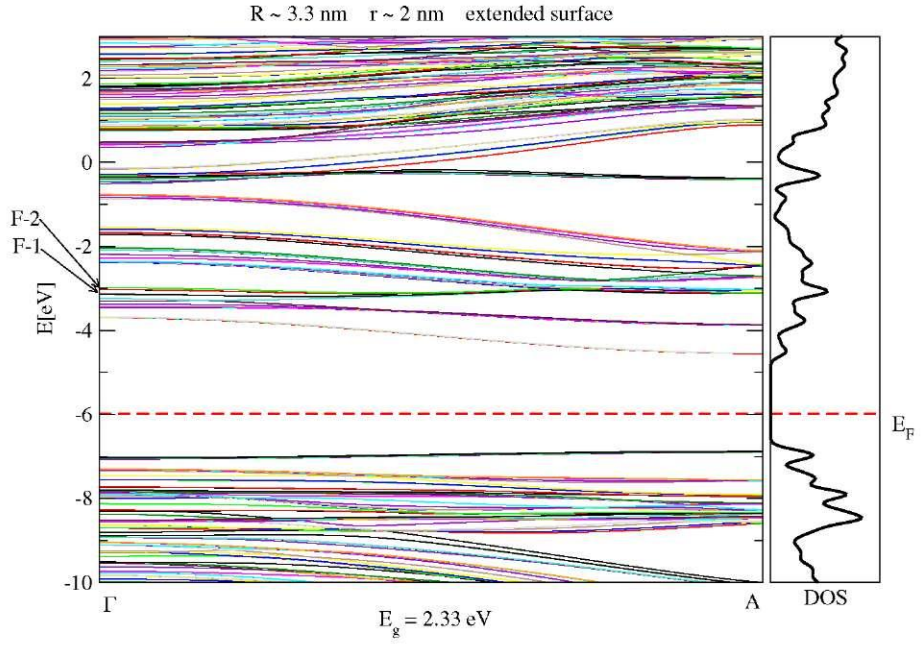

Figure 5.27: Band structure and DOS for the R = 3.3 nm, r = 2 nm nanotube endowed with a surface extended basis

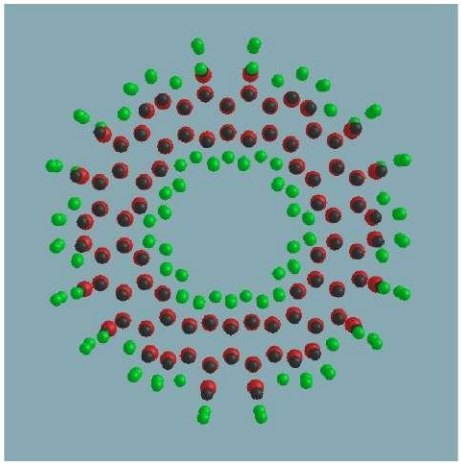

Figure 5.28: Atomic positions and locations of the additional surface extended basis (in green) for the R = 3.3 nm r = 2 nm nanotube

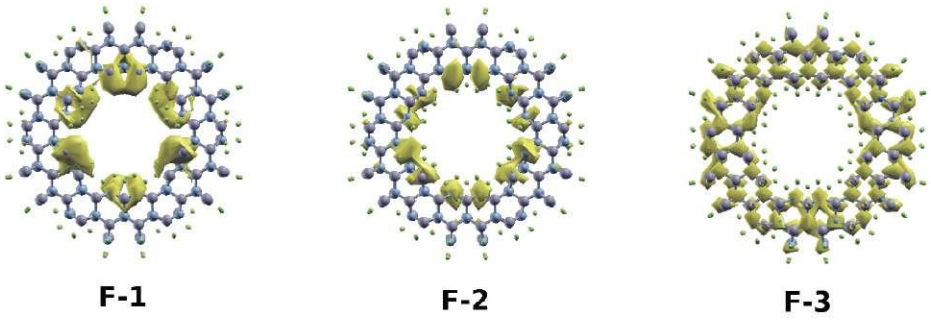

Figure 5.29: Two examples of surface localized wavefunctions (F-1 and F-2) and charge density distribution (F-3)

The most obvious effect of the inclusion of the additional basis functions is a total downshift in energy. Besides a somewhat more spatially spread out wavefunctions at the surface, no other significant effect can be noticed. It is interesting to observe the way in which the bandgap varies with the internal diameter, for a fixed external diameter, in both normal and surface extended base cases. An inversely proportional relation appears to exist between the internal diameter and the bandgap value. The effect of the augmented basis is a lowering in bandgap energy.

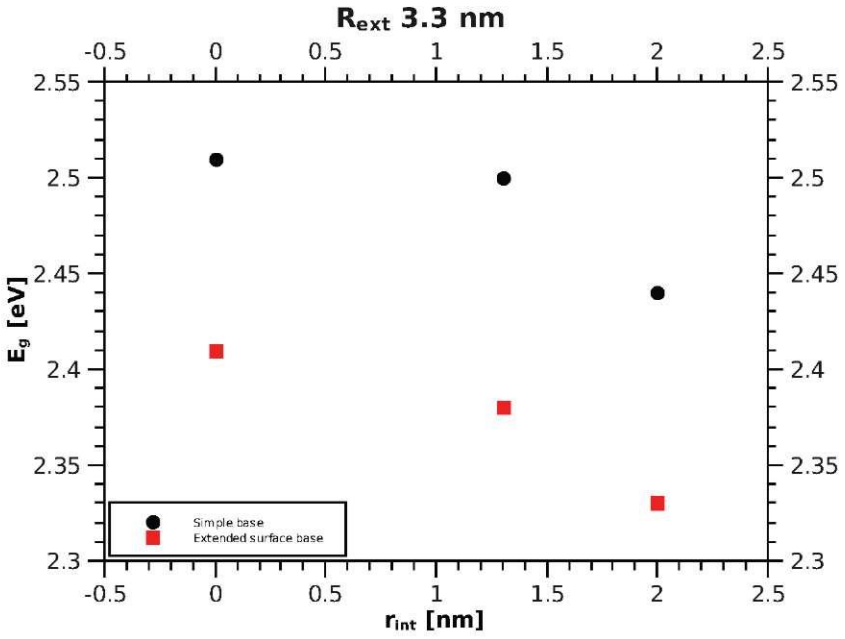

Figure 5.30: Bandgap variation with internal tube diameter (black-normal base; red-surface extended base)

An attempt was made at establishing the properties of a larger diameter nanotube with R = 5 nm and r = 3.6 nm. Because during the lattice relaxation it switched from the würtzite to the complex double walled graphene-like nanotube structure (Fig.5.32), it's properties fail to completely resemble those of the structures mentioned so far, in that

although new states do appear in the bulk bandgap, they overlap those from the valence and conduction bands (Fig.5.31). It will be further seen that this band structure resembles that of zig-zag and armchair graphene-like nanotubes although the bandgap value is still closer to that of würtzite nanotube; this bandgap value is expected to increase if the structure would be relaxed further.

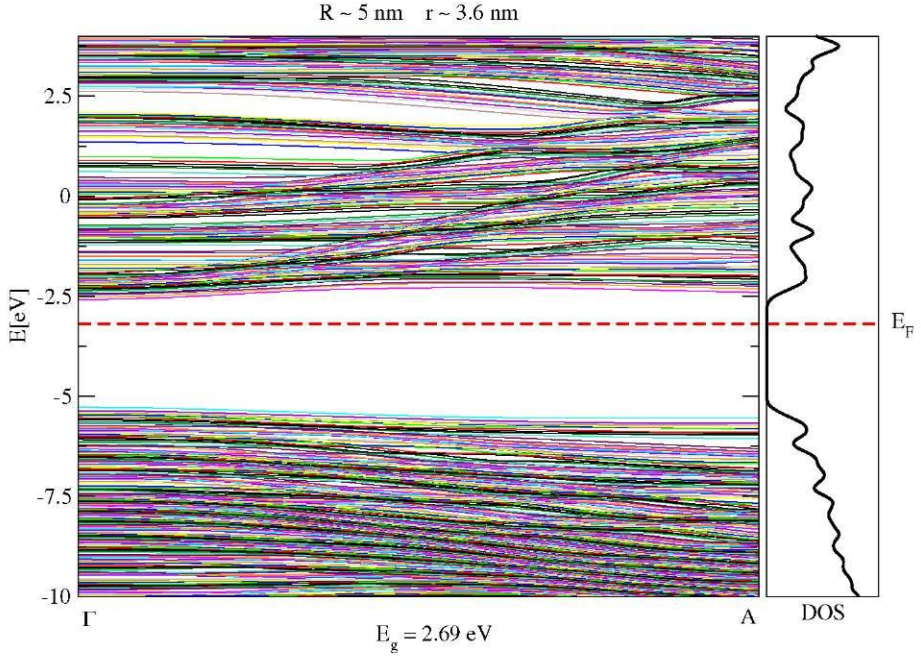

Figure 5.31: Band structure and DOS for the R = 5 nm, r = 3.6 nm nanotube

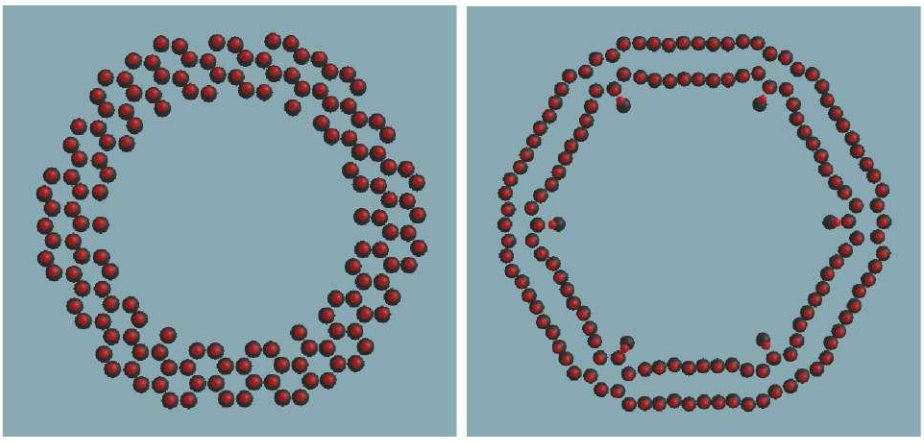

Figure 5.32: Initial and relaxed atomic positions for the R = 5 nm, r = 3.6 nm nanotube

The next two examples are those of nanotubes similar in structure to single walled carbon nanotubes and the main purpose for their investigation is to further confirm the validity of the results by comparing their properties with other numerical simulations and experimental data. The two structures chosen where that of a hexagonal zig-zag BN nanotube (Fig.5.34) with a diameter of 0.94 nm and a hexagonal armchair nanotube (Fig.5.36) with a diameter of 0.82 nm. The bandgap values of both zig-zag (Fig.5.33) and armchair (Fig.5.35) nanotubes are found to be in good agreement with experimental results([31]) with a value of 4.23 eV in the case of the zig-zag structure and 4.45 eV for the armchair nanotube. A lack of any narrow mini-bands inside the bandgap can be seen, as in the case of the R = 5 nm r = 3.6 nm nanotube (Fig.5.31).

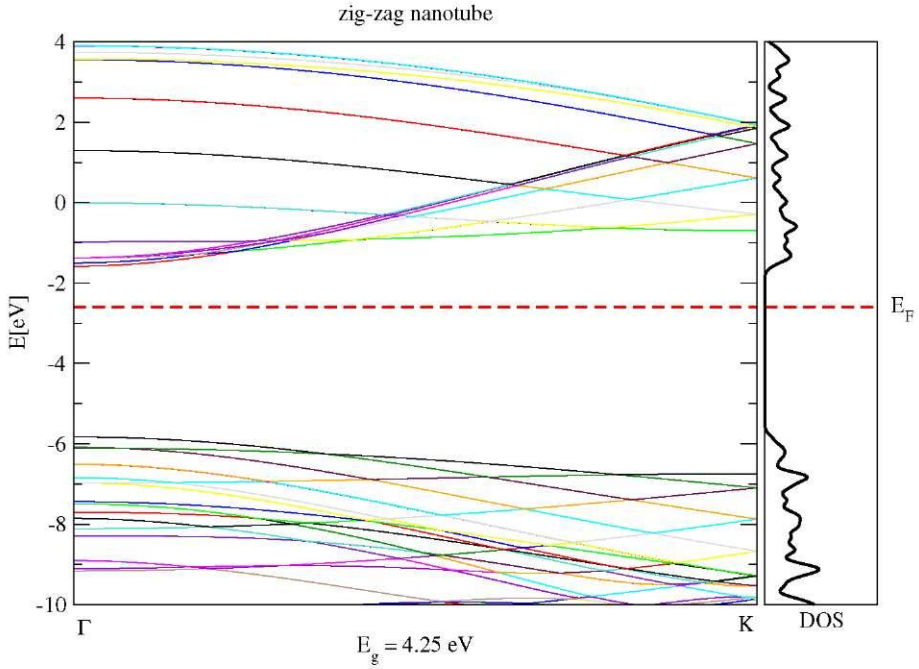

Figure 5.33: Bands structure of a graphene-like zig-zag BN nanotube

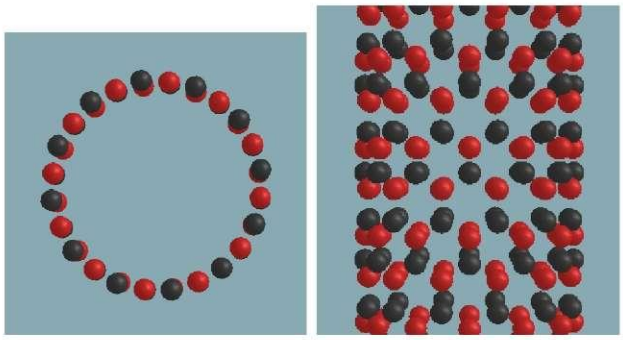

Figure 5.34: Initial and relaxed atomic positions for the graphene-like zig-zag BN nanotube

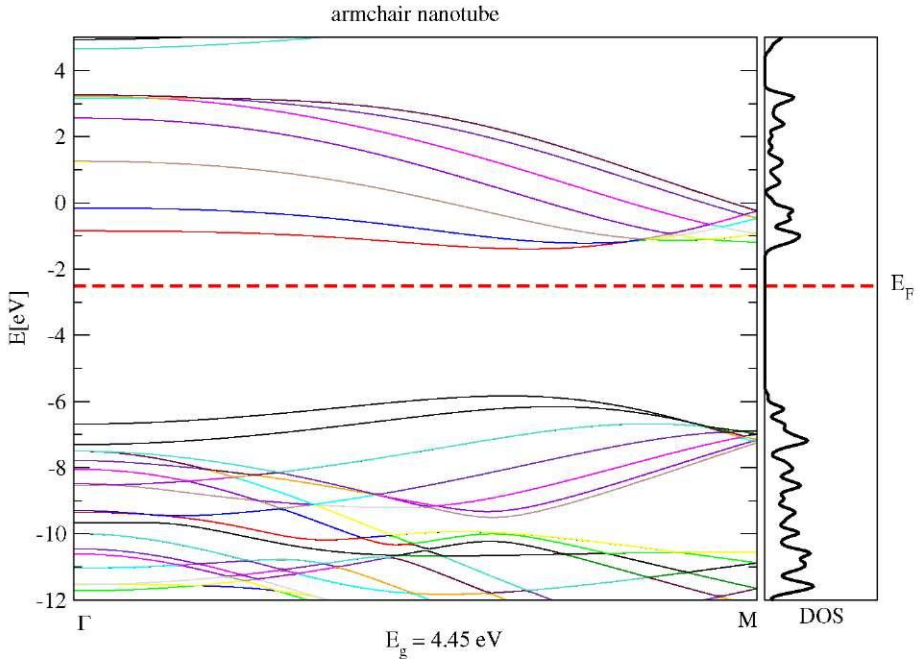

Figure 5.35: Bands structure of a graphene-like armchair BN nanotube

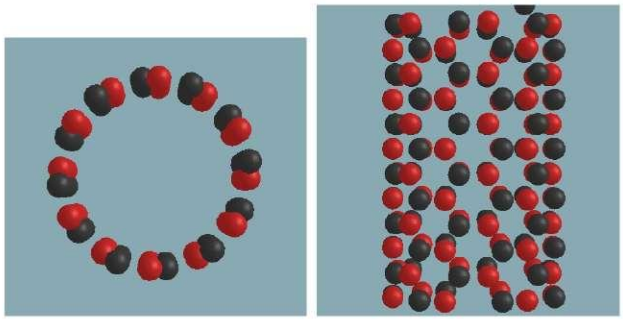

Figure 5.36: Initial and relaxed atomic positions for the graphene-like armchair BN nanotube

5.5 Stability of the structures

By comparing the energy per atom ratio for the different structures it is possible to identify those with a more stable structure, which also translates with a higher probability of being synthesized to the detriment of others.

Structure type	energy per atom [eV]
Bulk	-180.911
R − 2 nm r − 0 nm	-180.438
R 2 nm r 1 nm	-180.123
R − 3.3 nm r − 0 nm	-180.484
R 3.3 nm r 1.3 nm	-180.400
R − 3.3 nm r − 2 nm	- 180.221
R 3.3 nm r 0 nm e.s.*	-180.534
R − 3.3 nm r − 1.3 nm e.s.*	-180.469
R − 3.3 nm r − 2 nm e.s.*	-180.318
R − 5 nm r − 3.6 nm	-180.532
zig-zag	-180.692
armchair	-180.669

(* e.s. – enhanced surface which refers to the base being enhanced for the surface treatment; R – external radius, r – internal radius)

It can be seen that that the bulk crystal remains the most stable of them all; the zig-zag and armchair graphene-like structures come second; the largest nanotube (R − 5 nm, r − 3.6 nm) that switched from a würtzite type to a graphene-like nanotube structure, although it went through the least number of relaxation steps out of the entire set of structures, also shows a stable structure; out of the würtzite structures, the nanowires remain more stable than the nanotubes of similar external diameter and in the case of the tubular structures, the stability decreases with the increase of internal diameter.

5.6 Phonon dispersion

Another set of differences between q-1D structures and bulk BN material can also be seen by analyzing the phonon dispersion. Due to computational constraints, only some of the structures mentioned up until now have been studied further in this section. The method used to obtain the phonon dispersion was mentioned in Section 4.5 but an additional program entitled "vib2axsf", that was developed by Andrei Postnikov, and that is also part of the SIESTA package was used to graphically represent the first six phonon modes starting from frequency $0[cm^{-1}]$ upwards in order to have a visually clear proof of the differences between them; the reason for choosing the first six modes is just that these are the simpler ones to understand in terms of the motion of the constituent atoms.

In Fig.5.37 the BN bulk phonon frequencies (in the Γ point), as computed in [32], have been superimposed over a part of the phonon dispersion dispersion graph of the BN würtzite R − 2 nm nanowire. It can be clearly seen that a dramatic deviation from the bulk behavior takes place and that there is an almost continuous spectrum of modes up until $1250[cm^{-1}]$; this deviation from the reduced number of phonon modes found in the bulk material is an effect given by the 1D confination, the new symmetry of the system and surface relaxation effects that lifts the degeneracy of equivalent modes that can be found in the bulk material but also gives rise to new class of phonon modes without any bulk counterparts. An important observation is that the usual gap (for the dispersion along the Γ-A direction) between the bulk $LO_{\parallel}$ and $TO_{\perp}$ values vanishes. The phonon modes that can be found above the $1320[cm^{-1}]$ frequency appear due to the relaxation of the outer atomic layer (Fig.5.38) that leads to a higher force constant for between some of these atoms which translates to a higher frequency of oscillation for these surface phonons. The phonon modes found just above the $1350[cm^{-1}]$ appear to have nondisper-

sive behavior. The modes found above 1400$[cm^{-1}]$ are of a mixed type, with both atoms found on the surface and inside the nanowire taking part in the oscillation, but the major contribution is still that from surface. All the surface modes appear to have a longitudinal polarization, parallel to nanowire's optical axis, since the great majority of the atoms, but not all, oscillate in such a way.

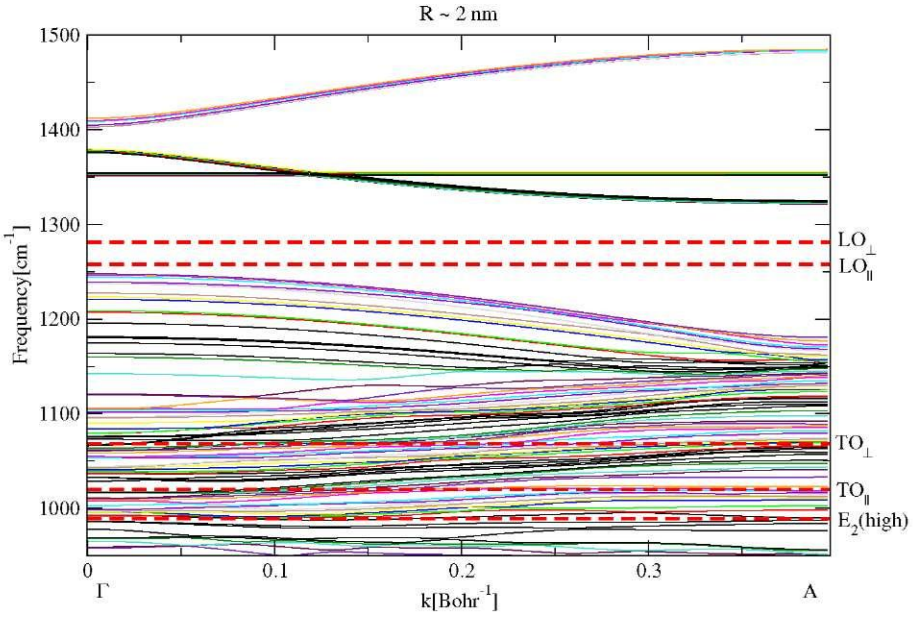

Figure 5.37: Phonon dispersion for R = 2 nm würtzite nanowire with superimposed bulk modes

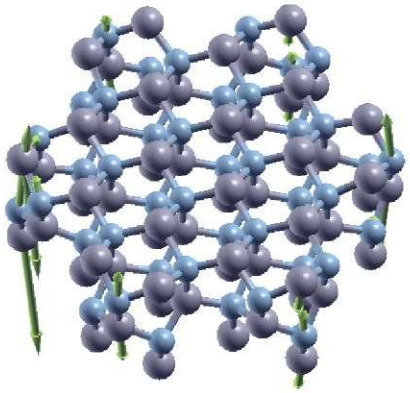

Figure 5.38: Graphical representation of force vector/atom for a surface phonon

In order to have a visual representation of the phonon modes found in a BN nanowire, the first six have been represented in Fig.5.39. Even amongst these very few number of modes there are examples of degeneracy lifting and new, confination deter-

mined, modes: the first three are the normal acoustic modes found in the bulk material that give rise to oscillations on the three axes, the fourth is an example of torsional acoustic-like vibration specific 1D structures, and the third and fourth are examples of longitudinal shear acoustic-like modes that deviate from the 'z' axis acoustic branch. These modes are being called acoustic-like because of the strong resemblance to the acoustic phonon modes where the neighbouring lattice ions move in phase, but since their frequency is not zero at a zero wavevector they are not strictly acoustic.

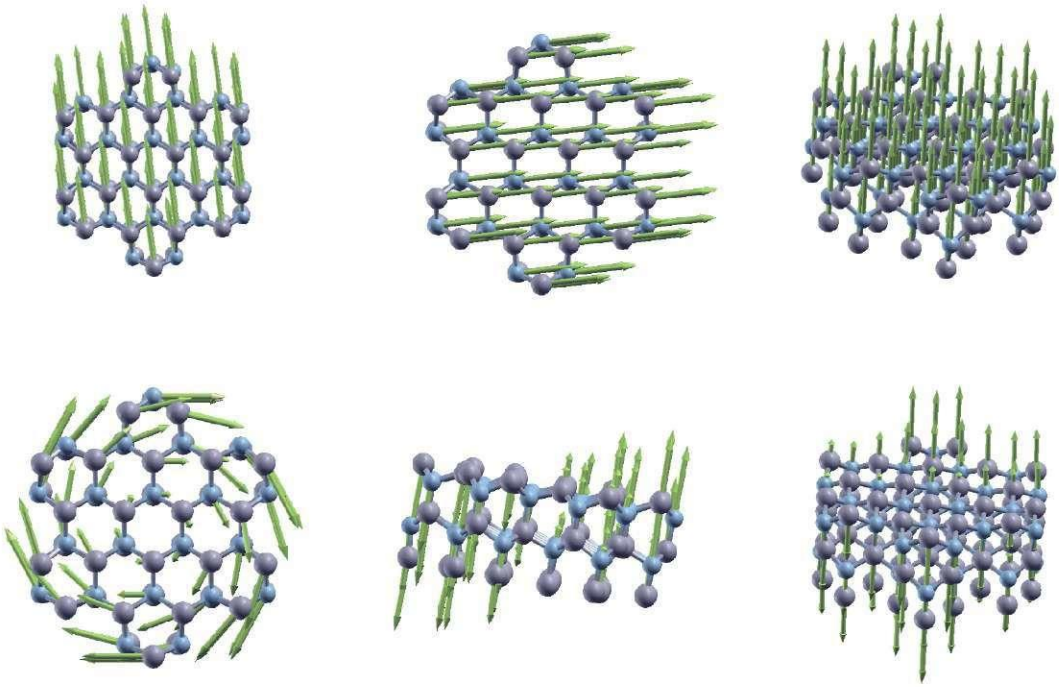

Figure 5.39: Graphical representation of force vector/atom for first six (from left to right) acoustic and acoustic-like modes in the R = 2 nm nanowire

The phonon dispersion behavior found for the R = 2 nm, r = 1 nm BN nanotube (Fig.5.40) is consistent with that of the R = 2 nm nanowire and shows obvious similarities. All the observations that were made for the phonon dispersion in the R = 2 nm nanowire also remain valid in this case. It is worth mentioning that, although the secondary surface alters the phononic behavior by producing a mini-band with a distinct dispersion characteristic in 1340-1342$[cm^{-1}]$ region, it is not possible to speak about phonons being localized on the interior or exterior surface because the surfaces of this tube are not easily distinguishable.

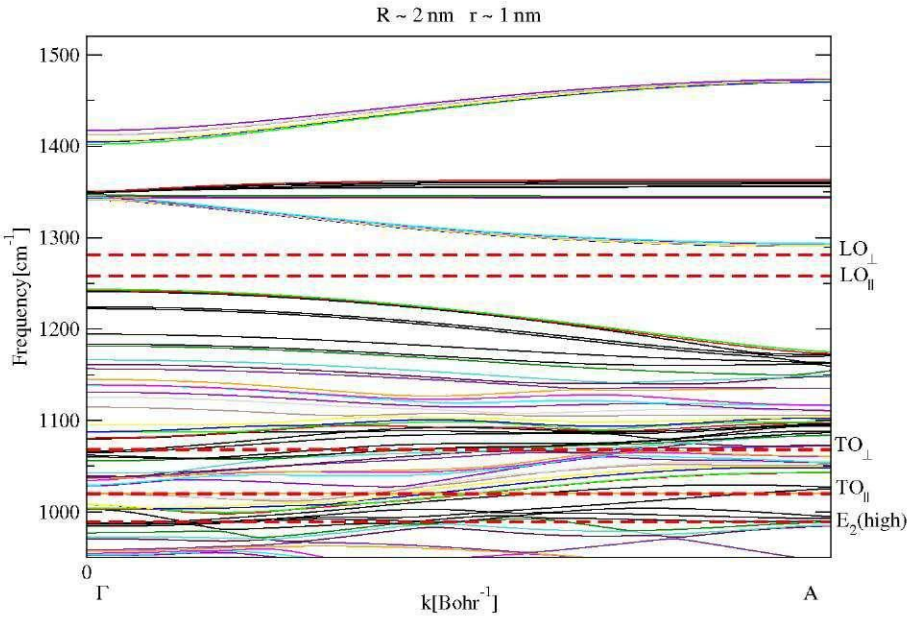

Figure 5.40: Phonon dispersion for R = 2 nm, r = 1 nm würtzite nanotube with superimposed bulk modes

What is noticeable in Fig.5.41 is that the shear modes for the nanotube are locates further up the frequency scale, being preceded by a series of oblong modes.

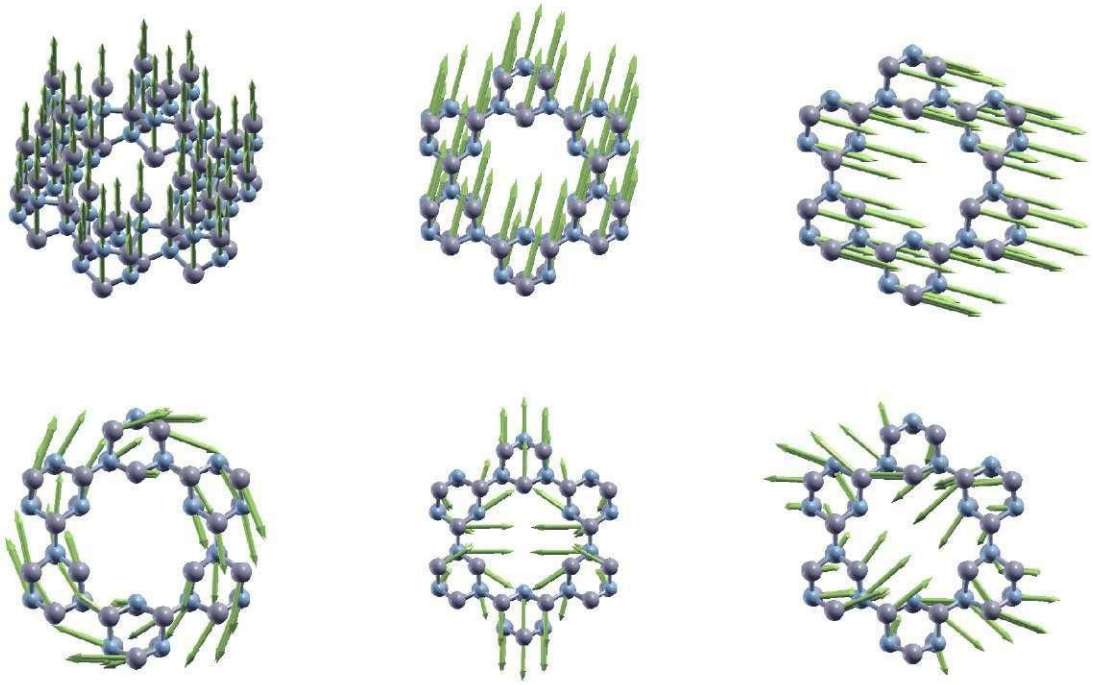

Figure 5.41: Graphical representation of force vector/atom for first six acoustic and acoustic-like modes in the R = 2 nm, r = 1 nm nanotube

The main difference between the two cases mentioned above and the phonon dispersion spectrum of the R = 3.3 nm, r = 1.3 nm is that a shift has taken place, raising the whole spectrum and placing the first surface phonon mode at 1390$[cm^{-1}]$. A

secondary, isolated, surface phonon band is located between 1807-1827$[cm^{-1}]$. As before, the surface phonon modes are characterized by a longitudinal polarization, parallel to the optical axis of the nanotube.

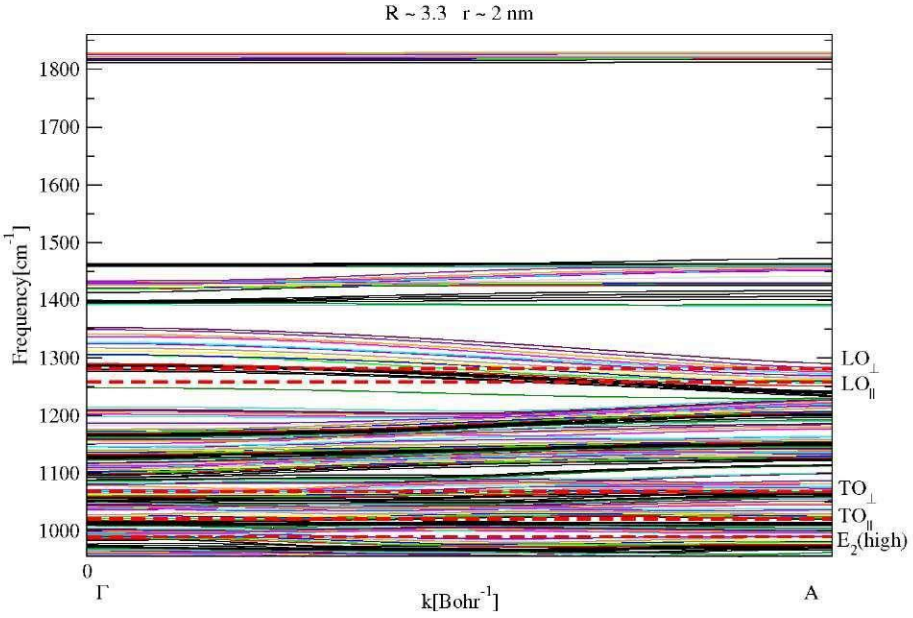

Figure 5.42: Phonon dispersion for R = 3.3 nm, r = 1.3 nm würtzite nanowire with superimposed bulk modes

In Fig.5.43 it can be observed that the first six modes are similar to the ones of the R = 2 nm, r = 1 nm nanotube (Fig.5.41) although their order seems to be changed; it is not known if this is a real effect or just an unwanted side effect of an incomplete lattice relaxation.

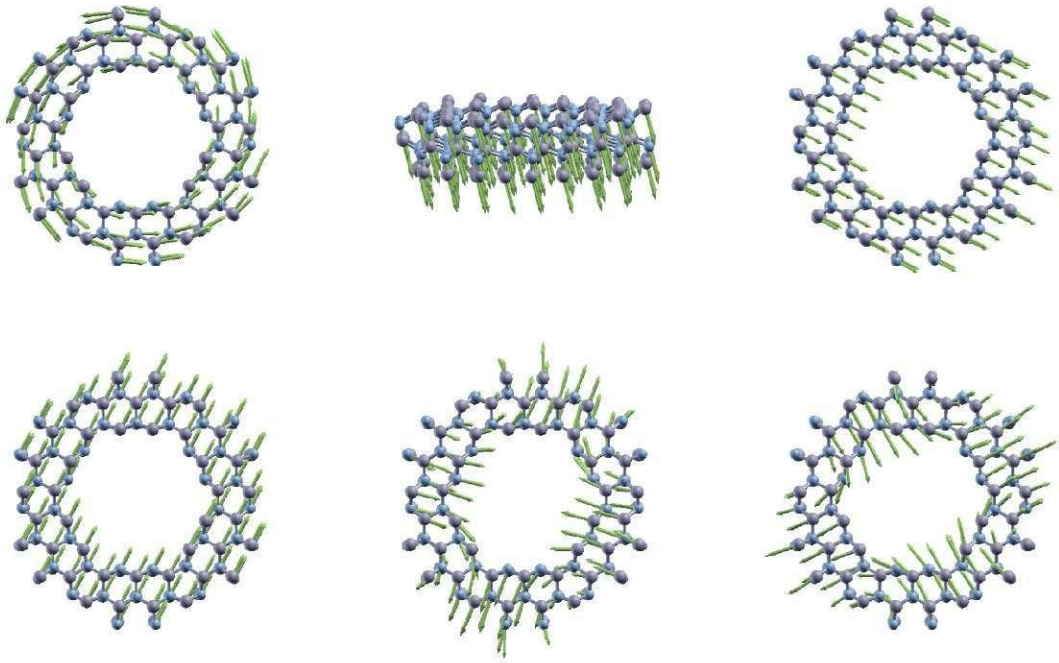

Figure 5.43: Graphical representation of force vector/atom for first six acoustic and acoustic-like modes in the R = 3.3 nm, r = 1.3 nm nanotube

The next two systems are those of a single layered graphene-like BN nanotube. Both the phonon dispersion spectra of zig-zag (Fig5.44) and of the armchair structure (Fig.5.46) appear to have little resemblance to that of the hexagonal BN sheet [33]. A resemblance between these two types of nanotubes is a very similar maximum frequency of 1550$[cm^{-1}]$ for the zig-zag tube and 1548$[cm^{-1}]$ for the armchair tube.

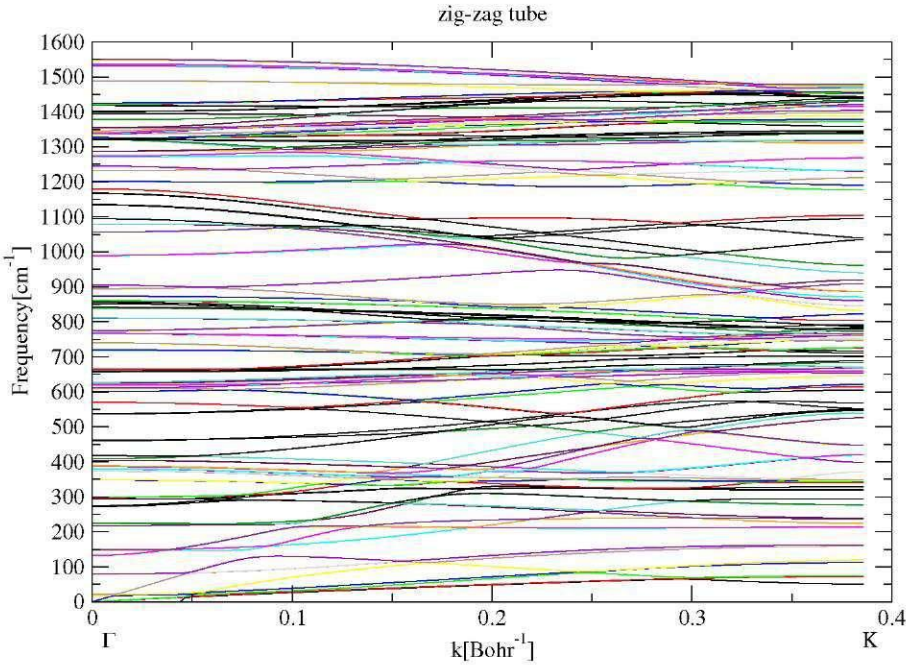

Figure 5.44: Phonon dispersion for zig-zag graphene-like nanotube

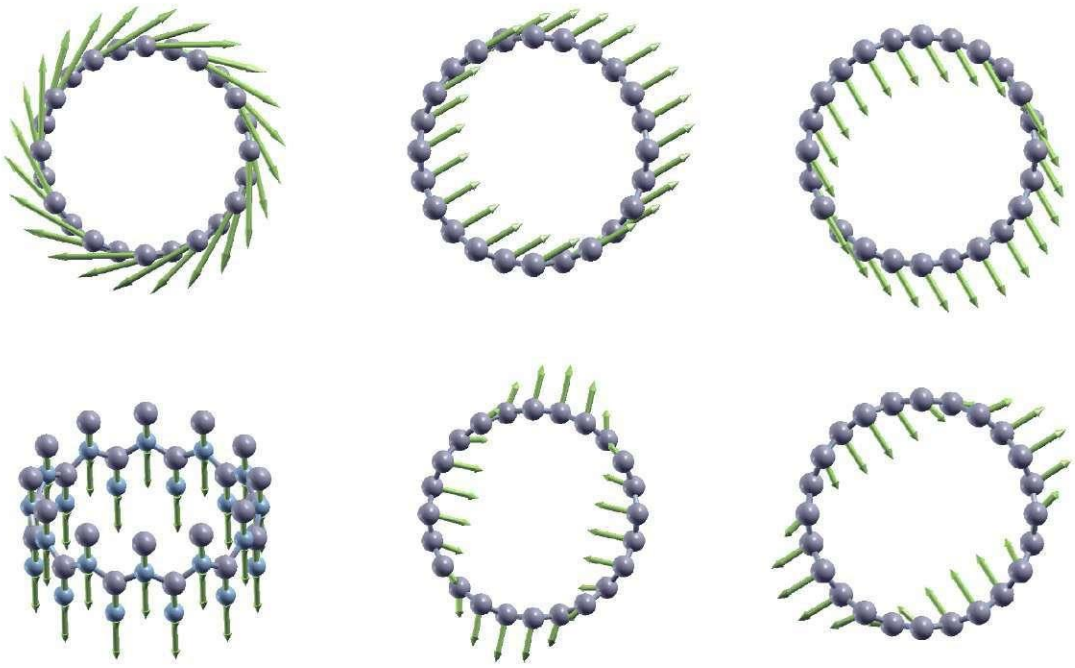

Figure 5.45: Graphical representation of force vector/atom for first six acoustic and acoustic-like modes in the zig-zag nanotube

The first six acoustic and acoustic-like phonon modes of the zig-zag (Fig.5.45) and armchair nanotubes (Fig.5.47) are similar, although they are not found in the same order; a peculiarity of the armchair nanotube is an elliptical torsional phonon mode. Both of these sets of six modes are similar to those found in the würtzite BN nanotubes (Fig.5.41 and Fig.5.43) but differ form the BN nanowire (5.39) revealing a similar feature of tubular structures.

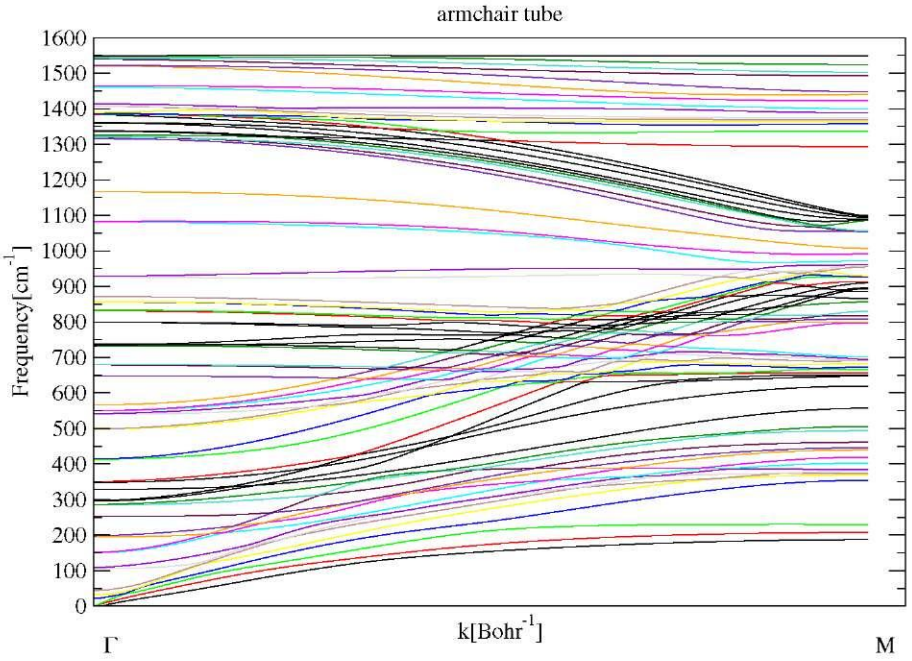

Figure 5.46: Phonon dispersion for armchair graphene-like nanotube

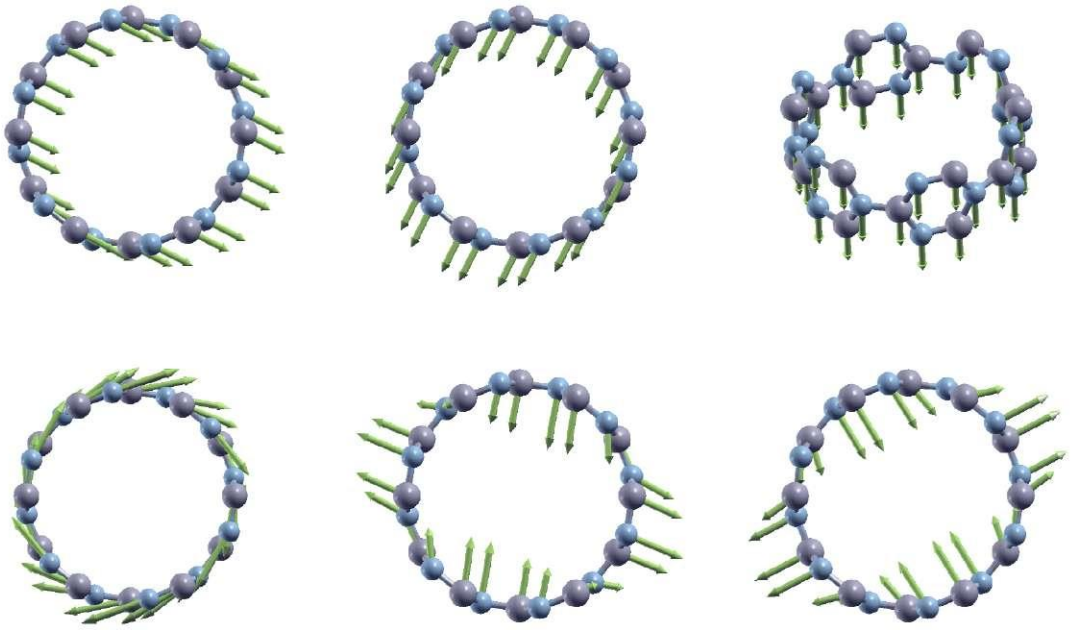

Figure 5.47: Graphical representation of force vector/atom for first six acoustic and acoustic-like modes in the armchair nanotube

Chapter 6

Conclusions and final remarks

A computational study has been carried out to reveal the differences that arise in the electronic and phononic properties of some selected q-1D structures when compared to the bulk material. Pseudopotentials have been constructed for the treatment of boron nitride.

The effects given by the surfaces have been investigated and it has been shown that for the q-1D structures new states appear in bandgap of the bulk material, and that these new states are located preponderantly on the exterior surface of both nanotubes and nanowires; this leads to a decrease of the effective bangap and thus points out to electronic and thermoelectric uses of the q-1D structures that would be inappropriate for the bulk würtzite BN isolator. An attempt has been made at obtaining better basis sets for the treatment of surfaces and the lower total energy achieved for the systems endowed with these kinds of bases has proven their use.

The stability of such structures has also been investigated showing that würtzite nanowires are more stable than nanotubes of same sizes and that graphene-like nanotubes are even more stable than both würtzite nanowires and nanotubes.

More dissimilarities between bulk BN and q-1D nanotubes and nanowires have been pointed out by a study of the phonon dispersion spectrum. The differences compared to the bulk system are discussed, revealing a multitude of new acoustic-like and optical phononic branches, which are a direct consequence of the q-1D character of the systems.

It must be stressed that the work presented here represents only a steeping stone towards more important results like: electron and phonon transport through q-1D structures, computing Seebeck coefficients and figures of merit of such devices, investigating electron-phonon interaction or the effects of dopant or magnetic impurities in nanowires and nanotubes.

Bibliography

[1] Quantum Monte Carlo and the CASINO program: highly accurate total energy calculations for finite and periodic systems - M. D. Towler

[2] Fundamentals of Density Functional Theory - Walter Kohn

[3] Electronic Structure - Basic Theory and Practical Methods - Richard Martin

[4] W. Kohn and L. J. Sham. Phys. Rev., 140:A1133 (1965)

[5] P. Hohenberg and W. Kohn. Phys. Rev., 136:B864 (1964)

[6] Implementation and Application of Advanced Density Functionals (PhD Thesis)- Michael Christopher Gibson (2006)

[7] P.W. Anderson. Science, 177:4047 (1972)

[8] R.O.Jones and O. Gunnarson. Rev. Mod. Phys. 51:689 (1989)

[9] D.M. Ceperley and B.J. Alder. Phys. Rev. Lett. 45:566 (1980)

[10] H. Hellmann. Jour. Chem. Phys. 3:61, 1935

[11] N. Troullier and J.L. Martins, Phys. Rev. B, 43:1993 (1991)

[12] S. Goedecker and K. Maschke. Phys. Rev. A, 45:89 (1992)

[13] Theoretical modeling of semiconductor surfaces: microscopic studies of electrons and phonons - G.P. Srivastava - World Scientific Publishing (1999)

[14] D.R. Hamann, M. Schlüter. and C. Chiang, Phys. Rev. Lett. 43, 1494 (1979)

[15] L. Kleinman and D.M. Bylander. Phys. Rev. Lett. 48:1426 (1982)

[16] P.E. Blöchl. 41:5414 (1990)

[17] X. Gonze, R. Strumpf and M. Scheffler, Phys. Rev. B 44:8503 (1991)

[18] J.M. Soler, E. Artacho et al. J. Phys.: Condens. Matter 14:2745 (2002)

[19] J.Junquera et al. Phys. Rev. B 64:235111 (2001)

[20] H.J. Monkhorst and J.D. Pack, Phys. Rev. B 13:5188 (1976)

[21] R.P. Feynman. Phys. Rev. 56:340 (1939)

[22] M. Born and J.R. Oppenheimer. Ann. Physik 84:457 (1927)

[23] Fizica solidului-partea I - D.E. Brancus - Ed. Universitatii din Bucuresti - 2000

[24] T. Zahn et al. Phys. Rev. Lett. 103:266803 (2009)

[25] H. Zhang et al. Nature Phys. 5:438 (2009)

[26] W. Shockley. Phys. Rev. 56:317 (1939)

[27] Sandra García-Gil et al. Phys. Rev. B 79:075441 (2009)

[28] K.T. Park, K. Terakura and N. Hamada, J. Phys. C:Solid State Phys. 20:1241 (1987)

[29] Christensen, N.E., I. Gorczyca, Phys. Rev. B 50:4397 (1994)

[30] Xu, Yong-Nian, W.Y. Ching Phys. Rev. B 44:7787 (1991)

[31] R.Czerw, S.Webster et al. Appl. Phys. Lett. 83:1617 (2003)

[32] Karch, K., F. Bechstedt, Phys. Rev. B 56:7404 (1997)

[33] Miyamoto, Y., L.M.L. Cohen, S.G. Louie, Phys. Rev. B 52:14971 (1995)

Personal statement

I would like to offer my sincere thank you to the people that helped me most during the last two years of study: to Conf. Dr. Lucian ION and Dr. Alexandru G. NEMNES for the many explanations, advices and patience that they have kindly bestowed upon me; to Prof. Dr. Stefan ANTOHE, the head of the MDEO research facility, for all his support and advices, and also for managing an efficient and well equiped work environment; to all the professors of the Faculty of Physics for sharing their pretious knowledge with us, the students; and last, but not least, i would like to thank all my colleagues for their support and friendship.